

# Quantum Noise Spectroscopy of Criticality in an Atomically Thin Magnet

Mark E. Ziffer<sup>1,2,3\*</sup>, Francisco Machado<sup>4,5†</sup>, Benedikt Ursprung<sup>2†</sup>,  
 Artur Lozovoi<sup>6,7†</sup>, Aya Batoul Tazi<sup>1†</sup>, Zhiyang Yuan<sup>6†</sup>, Michael E. Ziebel<sup>3</sup>,  
 Tom Delord<sup>7</sup>, Nanyu Zeng<sup>8</sup>, Evan Telford<sup>3</sup>, Daniel G. Chica<sup>3</sup>,  
 Dane W. deQuilettes<sup>9,10</sup>, Xiaoyang Zhu<sup>3</sup>, James C. Hone<sup>2</sup>, Kenneth L. Shepard<sup>8</sup>,  
 Xavier Roy<sup>3</sup>, Nathalie P. de Leon<sup>6</sup>, Emily J. Davis<sup>11</sup>, Shubhayu Chatterjee<sup>12\*</sup>,  
 Carlos A. Meriles<sup>7\*</sup>, Jonathan S. Owen<sup>3\*</sup>, P. James Schuck<sup>2\*</sup>,  
 Abhay N. Pasupathy<sup>1,13\*</sup>

<sup>1</sup>Department of Physics, Columbia University, New York, NY 10027 USA

<sup>2</sup>Department of Mechanical Engineering, Columbia University, New York, NY 10027 USA

<sup>3</sup>Department of Chemistry, Columbia University, New York, NY 10027 USA

<sup>4</sup>ITAMP, Harvard-Smithsonian Center for Astrophysics, Cambridge, MA 02138, USA

<sup>5</sup>Department of Physics, Harvard University, Cambridge, MA 02138, USA

<sup>6</sup>Department of Electrical and Computer Engineering, Princeton University,  
 Princeton, NJ 08540, USA

<sup>7</sup>Department of Physics, CUNY, The City College of New York, New York, NY, 10031, USA

<sup>8</sup>Department of Electrical Engineering, Columbia University, New York, NY 10027 USA

<sup>9</sup>Lincoln Laboratory, MIT, Lexington, MA, 02421, USA

<sup>10</sup>Center for Quantum Engineering, MIT, Cambridge, MA, 02139, USA

<sup>11</sup>Department of Physics, New York University, New York, NY 10003, USA

<sup>12</sup>Department of Physics, Carnegie Mellon University, Pittsburgh, PA 15213, USA

<sup>13</sup>Condensed Matter Physics and Materials Science Department,  
 Brookhaven National Laboratory, Upton, NY, 11973 USA

†These authors contributed equally

\*Corresponding author. Email: apn2108@columbia.edu, p.j.schuck@columbia.edu,  
 jso2115@columbia.edu, mz2733@columbia.edu, cmeriles@ccny.cuny.edu,  
 shubhayuchatterjee@cmu.edu

**Dynamic critical fluctuations in magnetic materials encode important information about magnetic ordering in the associated critical exponents. Using nitrogen-vacancy centers in diamond, we implement  $T_2$  (spin-decoherence) noise magnetometry to study critical dynamics in a 2D Van der Waals magnet CrSBr. By analyzing NV decoherence on time scales approaching the characteristic correlation time  $\tau_c$  of critical fluctuations, we extract the critical exponent  $\nu$  for the correlation length. Our result deviates from the Ising prediction and highlights the role of long-range dipolar interactions in 2D CrSBr. Furthermore, analyzing the divergence of the correlation length suggests the possibility of 2D-XY criticality in CrSBr in a temperature window near  $T_C$  where static magnetic domains are absent. Our work provides a first demonstration of  $T_2$  noise magnetometry to quantitatively analyze critical scaling behavior in 2D materials.**

Near criticality, the macroscopic properties of an ordered phase often display features that are directly related to its microscopic interactions (*1*). Notably, both static and dynamic correlations of the order parameter as a function of the physical parameter that tunes the transition, such as temperature or fields, exhibit universal scaling behavior near the critical point. Extracting the scaling functions and associated critical exponents can reveal a wealth of information about the microscopic interactions that lead to ordering, such as principal anisotropies, effective dimensionalities and interaction range (*1, 2*). In magnetic materials, key observables that exemplify such critical behavior are divergent correlation length ( $\xi$ ) and time ( $\tau_c$ ) of order parameter fluctuations (*2, 3*). The experimental characterization of fluctuation dynamics of magnetism has played key roles in understanding magnetic ordering in quantum materials, and in establishing the universality of critical phenomena (*3, 4*). At criticality magnetic order manifests in the form of fluctuating domains with sizes described by a spectrum of wavelengths  $\lambda = q^{-1}$  (where  $q$  is wavenumber). To extract a critical exponent, one requires experimental techniques that offer selectivity to fluctuations across a range of  $q$  to analyze variations in dynamics that are associated

with the divergence of the characteristic correlation length  $\xi$  (3).

The recent discovery of stable magnetic phases in atomically thin Van der Waals (VdW) crystals has introduced new platforms to study the rich phenomenology of 2D magnets, and address open questions regarding magnetism in a bona-fide 2D setting. (5). Unfortunately, atomically thin flakes of VdW magnets lack the sample volumes required to study magnetization dynamics using conventional techniques such as inelastic neutron scattering,  $\mu$ SR, NMR, and EPR (3). Quasi-elastic light scattering and magneto-optical techniques, recently applied to study critical fluctuations in 2D VdW magnets (6–8), are limited to probing very long wavelength fluctuations, which makes it challenging to resolve critical dynamics in the presence of static magnetic domains with dimensions below the optical diffraction limit.

Optically addressable solid-state spin-qubits are an emerging platform for sensing magnetism in mesoscopic materials, and can resolve fluctuations with wavelengths on the  $nm$  scale (9). Seminal studies with the NV center in diamond have used  $T_1$  relaxometry to probe fluctuations in condensed matter systems (10–13) including magnetic phases in 2D materials (14). However, NV  $T_1$  relaxometry achieves frequency tunability (in the GHz range) with the use of non-negligible external bias fields that may significantly alter the critical behavior in magnetic systems (10, 13). Furthermore, it is necessary to study the noise spectral density in the MHz to sub-kHz range to access critical dynamics on time scales comparable to the fluctuation correlation time  $\tau_c$  in many magnetic materials (3).

Recently it has been proposed that decoherence ( $T_2$  noise) spectroscopy with the NV center could be used to quantitatively analyze critical dynamics and extract critical exponents in mesoscopic 2D magnets (15). While  $T_2$  and  $T_2^*$  based noise sensing are applied extensively with the NV center to characterize the spectral density of low frequency noise ( $\sim$  kHz-MHz) from fluctuating nuclear and electron spins in the bulk and surface spin-bath in diamond, and from target molecules on the diamond surface (16–23), only recently has NV  $T_2$  noise sensing started to be employed to study fluctuations in magnetic phases of 2D condensed matter systems (24).

In this work, we experimentally demonstrate the capability of NV ensembles to characterize critical dynamics and scaling laws of fluctuation correlations in a 2D VdW magnetic material CrSBr (25). CrSBr is a VdW semiconductor with A-type layered antiferromagnetic (AFM) ordering below the bulk Néel temperature ( $T_N$ ) at  $\sim 132$ K (26–29). Below  $T_N$  the intralayer mag-

netic order is ferromagnetic (FM) with in-plane easy-axis ordering along the crystallographic  $b$ -axis, while interlayer AFM order forms along the  $c$ -axis from the stacking of individual layers with opposite intralayer FM magnetization (Figure 1a). In the thin film regime, even-number layers of CrSBr are purely AFM while odd-number layers possess a net magnetization from one uncompensated FM layer (30, 31).

We begin by using ensemble NV pulsed optically detected magnetic resonance (ODMR) (Figure 1a, Materials and Methods, & Fig S6) to image the stray magnetic fields from a tri-layer CrSBr flake (Figure 1a,b). Measurements are performed with a small external bias field ( $\sim 3.5$  mT) aligned along the NV spin quantization axis such that  $|m_s = 0\rangle \rightarrow |m_s = -1\rangle$  resonances associated with one orientation of NV centers in the ensemble are selectively addressed with microwave pulses (Materials and Methods 1.5). Figure 1d shows a stray field ( $B_{stray}$ ) image of tri-layer CrSBr at 100 K, along with an outline of the CrSBr flake determined from a simultaneously measured CrSBr photoluminescence image (Figure 1c, Materials and Methods 1.6) (32). As expected, we observe stray fields at the edges of the CrSBr flake consistent with in-plane magnetization along the  $b$ -axis from an uncompensated 2D FM layer (30, 31, 33). The stray field image agrees with the simulated projection of the stray field from a single FM layer of CrSBr onto the NV spin-quantization axis measured in our ensemble (Figure 1e and Fig S9).

## Identifying Critical Behavior with DC and $T_2$ Magnetometry

Next, we study the magnetic phase transition by imaging  $B_{stray}$  as a function of temperature with pulsed ODMR. Figure 2a shows the evolution of several representative stray field images across the phase transition. We observe the evolution of stray fields from an apparently uniformly magnetized domain below 132 K (Figure 1d and Figure 2a) to stray field patterns with  $\mu\text{m}$ -scale broken regions persisting over a temperature range of  $\sim 10$  K (Figure 2b,c) before the stray field signal disappears at  $\sim 142$  K (Figure 2d). The broken stray field patterns in the range of 132–142 K are consistent with  $\mu\text{m}$  scale magnetic domains that were observed to form across the phase transition in few-layer CrSBr with magnetic force microscopy and scanning single NV microscopy (30, 31). The structure of these domains has been attributed to spatial variations in strain that affect the interlayer exchange coupling (30, 31). To study the loss of

magnetization across the phase transition, we define a region of pixels from one large-scale domain (Figure 2e, inset) and track the average absolute value of the stray field  $\langle |B_{stray}| \rangle$  as a function of temperature. Figure 2e shows the temperature dependence of  $\langle |B_{stray}| \rangle$  from which we identify a characteristic phase transition temperature at  $\sim 140$  K. We refer to this temperature as  $T_C$  (as opposed to  $T_N$ ), as numerous studies on CrSBr have identified a characteristic temperature range where intralayer ferromagnetic correlations persist above  $T_N$  (25, 27, 28). We point out that the small increase in  $\langle |B_{stray}| \rangle$  at  $\sim 132$  K may be related to the development of such ordering dominated purely by intralayer FM correlations (25).

To further study the phase transition, we correlate the temperature dependent static magnetic imaging with magnetic fluctuations measured by NV spin-echo decoherence. To this end, we prepare the NV spin in a coherent state  $|\psi\rangle = (|0\rangle + |-1\rangle)/\sqrt{2}$ , and allow it to evolve for a time period  $\tau$  under the fluctuating magnetic field, such that  $|\psi(\tau)\rangle = (|0\rangle + e^{-i\phi(\tau)}|-1\rangle)/\sqrt{2}$ . We then evaluate the coherence decay  $C(\tau) = e^{-\langle \phi^2(\tau) \rangle / 2}$ , where  $\langle \phi^2(\tau) \rangle$  is the variance of the stochastic phase over multiple experimental runs (Figure 3a) (15, 23). The stochastic phase variance  $\langle \phi^2(\tau) \rangle$  can be related to the noise spectral density from magnetic fluctuations  $N(\omega)$  sensed by the NVs (15):

$$\langle \phi^2(\tau) \rangle = \int_{-\infty}^{\infty} \frac{d\omega}{2\pi} W_{\tau}(\omega) N(\omega) \quad (1)$$

Here,  $W_{\tau}(\omega)$  is a spectral filter function that depends on the free evolution period  $\tau$  and is determined by the control pulse sequence (Figure 1a), which for spin-echo is:  $W_{\tau}(\omega) \propto \sin^4(\omega\tau/4)/\omega^2$  (15). For a fixed pulse sequence and NV depth distribution, changes in the decay of the coherence can thus be related directly to changes in the spectral density of the magnetic noise.

We perform spin-echo measurements at the center of the flake where  $\langle |B_{stray}| \rangle$  is evaluated (indicated approximately by the black circle in Figure 2c, see Materials and Methods 1.6). To quantify decoherence due to fluctuations from CrSBr we define a temperature normalized coherence:

$$C_{T_{Norm}}(\tau) = \frac{C_T(\tau)}{C_{T_{Ref}}(\tau)} = e^{-\langle \phi^2(\tau) \rangle_{T_{Norm}} / 2} \quad (2)$$

$$\langle \phi^2(\tau) \rangle_{T_{Norm}} = \langle \phi^2(\tau) \rangle_T - \langle \phi^2(\tau) \rangle_{T_{Ref}} \quad (3)$$

where the spin-echo decays  $C_T(\tau)$  and  $C_{T_{Ref}}(\tau)$  are measured at the same location on the

CrSBr flake at temperature  $T$  and a reference temperature  $T_{Ref}$ , respectively. Assuming that noise from the diamond spin bath adds a temperature independent background to  $\langle\phi^2(\tau)\rangle_T$  and  $\langle\phi^2(\tau)\rangle_{T_{Ref}}$  in the range of temperatures across the CrSBr phase transition,  $\langle\phi^2(\tau)\rangle_{T_{Norm}}$  then quantifies the decoherence contributed solely from relative temperature dependent differences in the noise spectral density from fluctuations in CrSBr (34).

Figure 3b shows  $C_{T_{Norm}}(\tau)$  for a range of temperatures across the CrSBr phase transition normalized with  $T_{Ref} = 131$  K. A dramatic increase in the rate of coherence loss can be observed as  $T$  approaches  $\sim 139$  K from temperatures both above and below  $T_C$ . We note that the temperature normalization fixes  $C_{T_{Norm}}(\tau)$  at  $\tau = 0$  to  $C_{T_{Norm}}(0) = 1$  for temperatures within the range of  $130 - 142$  K (taking into account both our Rabi frequency and inhomogeneous broadening of the NV ensemble, see Supplementary Text 2.1). As such, we fit the data in this temperature range to a stretched exponential function  $e^{-\left(\frac{\tau}{T_2}\right)^p}$  (Figure 3b), with  $\frac{1}{T_2}$  defined here as a decoherence rate due to the changes in magnetic noise from fluctuations in CrSBr as temperature is varied relative to  $T_{Ref}$  (35). Using the fit values for  $\frac{1}{T_2}$  we further determine a temperature weighted decoherence rate  $\frac{1}{TT_2}$  which increases monotonically with the uniform magnetic susceptibility ( $\chi_u$ ) of CrSBr (15). Figure 3c shows  $\langle|B_{stray}|\rangle$  plotted alongside  $\frac{1}{TT_2}$  for temperatures across the phase transition, from which we can precisely determine  $T_C = 138.75$  K based on the peak of  $\frac{1}{TT_2}$  that indicates the divergence in  $\chi_u$  at a continuous transition. The trend of  $\frac{1}{TT_2}$  shows a temperature range of critical fluctuations that spans from  $\sim 136.5 - 141$  K (Figure 3d).

We also extract the stretch power  $p$  from the fits to  $C_{T_{Norm}}(\tau)$ . Interestingly, the extracted  $p$  exhibits a peak within the temperature range of critical fluctuations highlighting a concurrent change to the functional form of the decoherence signal (Figure 3d, inset). This is made apparent by plotting  $\langle\phi^2(\tau)\rangle_{T_{Norm}}$  vs.  $\tau$  on a log-log scale for temperatures in the range of critical fluctuations. In Figure 3d,  $\langle\phi^2(\tau)\rangle_{T_{Norm}}$  shows a temperature dependent behavior near  $T_C$  that can be explained by the evolution of the noise spectral density due to critical slowing down of the fluctuation correlation time  $\tau_c$  (2, 15). At temperatures sufficiently far from criticality, scanning the spin-echo filter function  $W_\tau(\omega)$  over the experimental range of  $\tau$  samples a nearly flat region of the noise spectrum (blue trace, Figure 3e). Here, the resulting power law scaling of  $\langle\phi^2(\tau)\rangle$  over the range of  $\tau \sim 0.1 - 10 \mu s$  (blue trace, Figure 3f) is essentially temperature

independent, as the characteristic frequency of the noise spectral density ( $\omega_c = \tau_c^{-1}$ ) is in the range of  $\gtrsim$  GHz . However, as critical slowing down of  $\tau_c$  causes  $\omega_c$  to enter the  $\sim$  MHz range near  $T_C$  (red trace, Figure 3e), the filter function  $W_\tau(\omega)$  scans across a steep rise in the noise spectral density at low frequency and the power law scaling of  $\langle \phi^2(\tau) \rangle$  becomes sensitive to the temperature dependence of  $\tau_c$  (red trace, Figure 3f). If we define  $\langle \phi^2(\tau) \rangle = 2 (\tau/T_2)^p$  based on a stretched exponential model, then a temperature dependent change in the power law scaling of  $\langle \phi^2(\tau) \rangle$  corresponds to an observed change in  $p$  (15, 23).

## Analysis of Critical Dynamics and Determination of $\nu$

Having identified a temperature window indicating critical slowing down (Figure 3d), we proceed to analyze the decoherence dynamics to determine a critical exponent. The noise spectral density  $N(\omega)$  experienced by a single spin-qubit at a distance  $d$  below the 2D flake is determined by the dynamical structure factor  $S(q, \omega)$  that describes spatio-temporal fluctuations of the magnetic order parameter, and a momentum filter function  $W_d(q) \propto q^3 e^{-2qd}$  that determines the sensitivity of the spin-qubit to fluctuations with momentum  $q$  (15):

$$N(\omega) = \int_0^\infty W_d(q) S(q, \omega) \frac{dq}{2\pi} \quad (4)$$

We use a mean-field structure factor  $S(q, \omega)$  for critical behavior of non-conserved order parameters, consistent with the anisotropies in the CrSBr Hamiltonian (2, 15, 36, 37):

$$S(q, \omega) = \frac{2k_B T \Gamma_0}{\Gamma_0^2 J^2 (\xi^{-2} + q^2)^2 + \omega^2} \quad (5)$$

Here,  $J$  is the exchange energy,  $\Gamma_0$  is a “kinetic coefficient” which is related to a characteristic low temperature fluctuation frequency  $\omega_0$  (Supplementary Text 2.2.1), and  $\xi$  is the correlation length (15). Critical fluctuations are determined by the divergence of  $\xi$ , which exhibits a power-law scaling near  $T_C$ :

$$\xi = \xi_0 \left| \frac{T - T_C}{T_C} \right|^{-\nu} \quad (6)$$

where  $\nu$  is the critical exponent and  $\xi_0$  is a low temperature correlation length estimated from the CrSBr lattice constant (Supplementary Text 2.2.1) (15). Using Eqs (1-6) and a probability distribution function for NV depths in our ensemble we simulate an ensemble averaged

$\langle \phi^2(\tau) \rangle_{T_{Norm}}$  (Supplementary Text 2.2.1) with  $T_{Ref} = 136.75 \text{ K}$  over the temperature window of critical slowing down (Figure 4a, also see Figure 3d inset, red dashed trace) (38).

To determine the parameters  $\nu$ ,  $\omega_0$ , and  $J$ , the simulation is globally fit to the temperature dependent data in Figure 4a with  $T_C$  fixed at 138.75 K as determined from the  $\frac{1}{TT_2}$  peak (Figure 3c). The resulting best fit value for  $\omega_0 = 15.71 \text{ GHz}$  is in good agreement with the scale of magnon frequencies measured in CrSBr at low temperatures ( $\sim 20 - 30 \text{ GHz}$ ) (39, 40) and the value for  $J = 7.5 \text{ meV}$  agrees with theoretical and experimental expectations for exchange constants in CrSBr (25, 29). Turning our attention to the critical exponent, the best fit model gives a value  $\nu = 0.73$ . CrSBr is characterized by in-plane ferromagnetic order with magnetocrystalline anisotropy that favors easy-axis ordering along the  $b$  axis (27, 36, 41); from this perspective, the critical behavior would be expected to fall under a 2D Ising transition where  $\nu_{Ising} = 1$ . However, we find that fitting with  $\nu_{Ising}$  poorly reproduces the trends in the data (grey traces, Figure 4a), and the data can only be modelled using values of  $\nu$  in the range of  $\sim 0.6 - 0.8$  (Fig S13).

One explanation for the deviation of  $\nu$  from the Ising value is the presence of long-range dipolar interactions, which are known to be important for capturing the small- $q$  magnetization dynamics in bulk CrSBr at low temperatures (39). Indeed, long-range dipolar interactions are also known to modify critical dynamics away from the predictions from exchange-only models (3), with isotropic long-range interactions leading to a reduced value of  $\nu$  (42, 43). From this perspective, our results suggest that the effects of long-range dipolar interactions that influence magnetization dynamics in bulk CrSBr (39) also extend to the 2D, few layer limit. Furthermore, it is important to note that both the easy-axis magnetocrystalline anisotropy and the dipolar interaction are quite small compared to both the XY exchange interaction in CrSBr and deviation from the critical temperature  $\Delta T = T - T_C$  in the temperature window where we measure critical slowing down (Figure 3d) (36, 39). In fact, evidence suggesting that the transition may be characterized by 2D XY criticality has been previously reported (26, 29). To this end, we can compare our simulation results with expectations for XY-type critical behavior by evaluating the temperature dependence of the correlation length  $\xi$ . For the topological BKT transition associated with a 2D XY magnet,  $\xi_{BKT} = \xi_0 e^{b/\sqrt{(T-T_C)/T_C}}$  diverges exponentially as  $T \rightarrow T_C$  rather than following a power law (44–46). In the temperature window near  $T_C$  from our simu-



lations, we find that  $\xi_{BKT}$  indeed falls within the range of behavior for the power law divergence of  $\xi$  from Eq (6) with  $\nu \sim 0.6 - 0.8$  (Figure 4a, inset). However, very close to  $T_C$ , the exponential divergence of  $\xi_{BKT}$  is likely to be affected by the presence of static domains on the  $\lesssim 100$  nm length scale, which we believe form in our sample near criticality (Supplementary Text 2.1) (31). To fully characterize the universality class of the magnetic transition, further studies would be needed to correlate fluctuation dynamics with the static domain structure on the nano-scale.

Finally, we explicitly determine the slowing down of the fluctuation correlation time by evaluating the structure factor at temperatures near criticality using the best fit parameters for  $\nu$ ,  $\omega_0$ , and  $J$  with  $T_C = 138.75$  K. Figures 4b,c show the structure factor evaluated from Eq (5,6) at  $137.25$  K and  $138$  K, along with a contour of the characteristic frequency  $\omega_c(q)$ , which corresponds to the inverse of the fluctuation correlation time  $\tau_c(q)^{-1}$  (Supplementary Text 2.2). A comparison between the  $\tau_c(q)^{-1}$  contours at  $137.25$  K and  $138$  K clearly demonstrates critical slowing down of the fluctuation correlation time in the range of small- $q$  probed by our NV ensemble. In particular, the correlation time at  $138$  K (Figure 4c) starts to fall directly into the window of the free evolution times  $\tau$  in our spin echo experiments, highlighting that the trends in the decoherence dynamics that we observe at criticality (Figure 3d) are indeed consistent with theoretical expectations for the critical slowing down of fluctuations in CrSBr.

## Concluding Remarks and Outlook

Our work constitutes a first foray into the quantitative analysis of critical phenomena in 2D materials using NV  $T_2$  noise spectroscopy. As such, it highlights some crucial challenges and opportunities as this technique becomes more widely adopted. First, the form of  $\langle \phi^2(\tau) \rangle$  is sensitive to the NV ensemble depth distribution (Supplementary Text 2.2.2), highlighting the need for ensembles with precise NV depth distributions (e.g. delta doped ensembles (23)). Moreover, techniques such as noise co-variance magnetometry may be advantageous as they rely on directly measuring fluctuation correlations between two spatially precise single NVs, avoiding the need to analyze fluctuation spatial correlations based solely on NV depths and associated  $q$ -space filter functions (47). Second, we note that pulse sequences with filter functions that give

higher spectral resolution (e.g. XY-8, CPMG) are desirable to better resolve the noise spectral density. In particular, structure factors are known to deviate significantly from mean-field models at temperatures very close to  $T_C$  (1, 3), which could explain the trend in our data between  $138.25\text{ K} - 138.75\text{ K}$  where the stretch exponent  $p$  and the decoherence rate  $\frac{1}{T_2}$  become anti-correlated approaching  $T_C$  (Figure 3d). Here, pulse sequence filter functions with high spectral resolution will be instrumental to characterize the more complex structure of  $N(\omega)$ .

## References

1. J. Cardy, *Scaling and Renormalization in Statistical Physics* (Cambridge University Press, Cambridge, 1996).
2. P. C. Hohenberg, B. I. Halperin, *Reviews of Modern Physics* **49**, 435 (1977).
3. E. Frey, F. Schwabl, *Advances in Physics* **43**, 577 (1994).
4. S. Sachdev, *Physics World* **12**, 33 (1999).
5. Y. Ahn, X. Guo, S. Son, Z. Sun, L. Zhao, *Progress in Quantum Electronics* **93**, 100498 (2024).
6. D. Lujan, *et al.*, *Nature Communications* **13**, 2527 (2022).
7. C. Jin, *et al.*, *Nature Materials* **19**, 1290 (2020).
8. X.-X. Zhang, *et al.*, *Nano Letters* **21**, 5045 (2021).
9. F. Casola, T. van der Sar, A. Yacoby, *Nature Reviews Materials* **3**, 17088 (2018).
10. C. Du, *et al.*, *Science* **357**, 195 (2017).
11. S. Hsieh, *et al.*, *Science* **366**, 1349 (2019).
12. T. I. Andersen, *et al.*, *Science* **364**, 154 (2019).
13. H. Wang, *et al.*, *Science Advances* **8** (2022).

14. M. Huang, *et al.*, *Nature Communications* **14**, 5259 (2023).
15. F. Machado, E. A. Demler, N. Y. Yao, S. Chatterjee, *Physical Review Letters* **131**, 070801 (2023).
16. A. Laraoui, *et al.*, *Nature Communications* **4**, 1651 (2013).
17. T. Staudacher, *et al.*, *Science* **339**, 561 (2013).
18. B. Myers, *et al.*, *Physical Review Letters* **113**, 027602 (2014).
19. T. Roskopf, *et al.*, *Physical Review Letters* **112**, 147602 (2014).
20. E. Schäfer-Nolte, *et al.*, *Physical Review Letters* **113**, 217204 (2014).
21. J.-P. Tetienne, *et al.*, *Nano Letters* **16**, 326 (2016).
22. B. L. Dwyer, *et al.*, *PRX Quantum* **3**, 040328 (2022).
23. E. J. Davis, *et al.*, *Nature Physics* **19**, 836 (2023).
24. R. Xue, *et al.*, *arXiv:2403.01057* (2024).
25. M. E. Ziebel, *et al.*, *Nano Letters* **24**, 4319 (2024).
26. S. A. López-Paz, *et al.*, *Nature Communications* **13**, 4745 (2022).
27. E. J. Telford, *et al.*, *Nature Materials* **21**, 754 (2022).
28. K. Lee, *et al.*, *Nano Letters* **21**, 3511 (2021).
29. A. Scheie, *et al.*, *Advanced Science* **9** (2022).
30. D. J. Rizzo, *et al.*, *Advanced Materials* **34**, 2201000 (2022).
31. M. A. Tschudin, *et al.*, *arXiv:2312.09279* (2023).
32. Here the stray field is defined as  $B_{stray} = B - B_{avg}$ , where the subtraction of the signal averaged over all pixels in the image ( $B_{avg}$ ) approximately removes the constant offset due to the external bias field (48).

33. T. S. Ghiasi, *et al.*, *npj 2D Materials and Applications* **7**, 62 (2023).
34. We note that similar normalization procedures to quantify a relative change in decoherence signal are used for other NV sensing techniques, e.g. DEER (22).
35. Note that  $\tau = T_2$  corresponds to the time at which the coherence signal has decayed to a fixed value of  $C(T_2) = e^{-2}$ , allowing for a fair comparison of the decoherence rate across coherence decays with different functional forms.
36. T. M. J. Cham, *et al.*, *Nano Letters* **22**, 6716 (2022).
37. B. I. Halperin, P. C. Hohenberg, *Physical Review* **177**, 952 (1969).
38. The  $\langle \phi^2(\tau) \rangle_{T_{Norm}}$  data and model in Figure 4a are normalized using a reference temperature near criticality ( $T_{Ref} = 136.75$  K), as we expect the mean-field derived structure function (Eq (5)) to describe fluctuations quantitatively only for a range of temperatures near criticality.
39. Y. Sun, *et al.*, *Nature Physics* (2024).
40. Y. J. Bae, *et al.*, *Nature* **609**, 282 (2022).
41. K. Yang, G. Wang, L. Liu, D. Lu, H. Wu, *Physical Review B* **104**, 144416 (2021).
42. N. Defenu, *et al.*, *Reviews of Modern Physics* **95**, 035002 (2023).
43. B. Sbierski, *et al.*, *Physical Review B* **109**, 144411 (2024).
44.  $b$  is typically a non-universal O(1) constant in the range of  $\sim 0.1 - 5$  (49, 50).
45. J. M. Kosterlitz, *Journal of Physics C: Solid State Physics* **7**, 1046 (1974).
46. J. V. José, L. P. Kadanoff, S. Kirkpatrick, D. R. Nelson, *Physical Review B* **16**, 1217 (1977).
47. J. Rovny, *et al.*, *Science* **378**, 1301 (2022).
48. Z. Kazi, *et al.*, *Physical Review Applied* **15**, 054032 (2021).

49. L. Vanderstraeten, B. Vanhecke, A. M. Läuchli, F. Verstraete, *Physical Review E* **100**, 062136 (2019).
50. M. M. Rams, P. Czarnik, L. Cincio, *Physical Review X* **8**, 041033 (2018).
51. S. Sangtawesin, *et al.*, *Physical Review X* **9**, 031052 (2019).
52. S. T. Alsid, *et al.*, *Physical Review Applied* **12**, 044003 (2019).
53. M. Posselt, J. Biersack, *Nuclear Instruments and Methods in Physics Research Section B: Beam Interactions with Materials and Atoms* **64**, 706 (1992).
54. N. Raatz, C. Scheuner, S. Pezzagna, J. Meijer, *physica status solidi (a)* **216** (2019).
55. E. Bauch, *et al.*, *Physical Review B* **102**, 134210 (2020).
56. L. Wang, *et al.*, *Science* **342**, 614 (2013).
57. D. B. Bucher, *et al.*, *Nature Protocols* **14**, 2707 (2019).
58. D. B. Durham, D. F. Ogletree, E. S. Barnard, *Surface and Interface Analysis* **50**, 1174 (2018).
59. C. S. Aitchison, *et al.*, *IEEE Transactions on Microwave Theory and Techniques* **19**, 928 (1971).
60. K. Gupta, R. Garg, R. Chadha, *Computer-Aided Design of Microwave Circuits* (Artech House, Inc., Dedham, MA, 1981).
61. J. R. Rabeau, *et al.*, *Applied Physics Letters* **88** (2006).
62. S. van der Walt, *et al.*, *PeerJ* **2**, e453 (2014).
63. M. Ortner, L. G. Coliada Bandeira, *SoftwareX* **11**, 100466 (2020).
64. A. Dréau, *et al.*, *Physical Review B* **84**, 195204 (2011).
65. J. F. Barry, *et al.*, *Reviews of Modern Physics* **92**, 015004 (2020).

66. A. Schweiger, G. Jeschke, *Principles of Pulse Electron Paramagnetic Resonance* (Oxford University Press, New York, 2001).
67. D. Puzzuoli, C. J. Wood, D. J. Egger, B. Rosand, K. Ueda, *Journal of Open Source Software* **8**, 5853 (2023).

## Acknowledgments

We thank Shaowen Chen, Nikola Maksimovic, Ruolan Xue, Laurens Vanderstraeten, Nick Bronn, Jennifer Schloss, Lin Pham, Mikael Backlund and Kristina Liu for fruitful discussions. We thank Daybis Tencio for obtaining the C-TRIM software and assisting in aspects of the sample preparation. NV magnetometry experiments and instrument development at Columbia were primarily supported by Programmable Quantum Materials, an Energy Frontier Research Center funded by the U.S. Department of Energy (DOE), Office of Science, Basic Energy Sciences (BES) under award no. DE-SC0019443. M.E.Z. acknowledges funding support from Columbia University's Research Initiatives in Science and Engineering competition. J.S.O. was supported by the National Science Foundation (NSF) under CHE-2004008. A.N.P. was supported by the Air Force Office of Scientific Research under grant FA9550-21-1-0378. A.B.T. was supported by the NSF under grant DMR-2004691. Work at Princeton was supported by the NSF (QuSEC-TAQS OSI 2326767 and Princeton University's Materials Research Science and Engineering Center DMR-2011750) and the Gordon and Betty Moore Foundation (grant DOI 10.37807/gbmf12237). T.D. acknowledges support by the DOE Office of Science, National Quantum Information Science Research Centers, Co-design Center for Quantum Advantage (C2QA) under contract number DE-SC0012704. A.L. and C.A.M. acknowledge support from the National Science Foundation, grant 1914945. C.A.M. also acknowledges support from the National Science Foundation, grant 2203904. F.M. acknowledges support from the NSF through a grant for ITAMP at Harvard University. S.C. acknowledges support from a PQI Community Collaboration Award.

## Author Contributions

M.E.Z. conceived of the project with A.N.P., P.J.S., and J.S.O. M.E.Z. performed the experiments and analyzed the data with F.M., E.J.D., and S.C. M.E.Z. built the experimental apparatus with assistance from B.U. and designed the experiments with A.L., T.D., and C.A.M. Z.Y. and N.P.dL. processed the diamond used for ensemble NV magnetometry and A.B.T. fabricated the CrSBr flake on the diamond. D.G.C., E.J.T., M.E.Z., and X.R. synthesized and provided CrSBr crystals. N.Z. and K.L.S. assisted with testing the microwave PCB. D.W.D. grew and provided NV ensemble samples for initial experiments to verify the setup. X-Y.Z. and J.C.H. provided equipment and resources for experiments. A.N.P., P.J.S., and J.S.O. supervised the work. M.E.Z., F.M., E.J.D., and S.C. wrote the manuscript. The manuscript reflects the contributions and ideas of all authors.

## Supplementary Materials

Materials and Methods

Supplementary Text

Figs. S1 to S13

References (51–67)

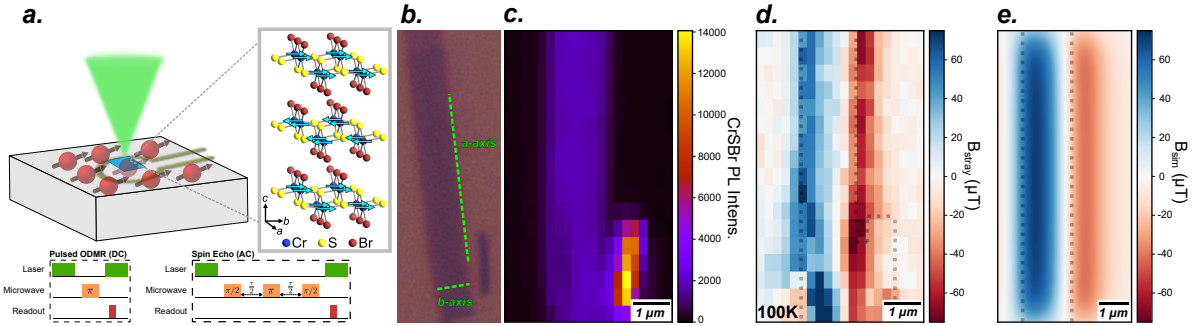


**Figure 1: Magnetic imaging of 2D CrSBr below  $T_C$ .** (a) Schematic of the experimental sample configuration with a CrSBr flake (blue rectangle) transferred onto the surface of a  $^{12}\text{C}$  diamond substrate with an NV ensemble (red spins) implanted at an average depth of  $\sim 50\text{nm}$  (Materials and Methods 1.1). (Inset) Atomic and magnetic structure of a CrSBr tri-layer, with turquoise arrows representing the magnetic moment on Cr atoms. Also shown are simplified pulse sequences for the DC and AC magnetometry techniques used in this work (see Fig S6 for full pulse sequences). (b) Brightfield optical image of the tri-layer CrSBr flake on a  $\text{SiO}_2(285\text{ nm})/\text{Si}$  substrate. (c) Photoluminescence image (measured at  $100\text{ K}$ ) of the tri-layer CrSBr flake transferred onto the diamond substrate. The bright region in the lower right corresponds to another small multilayer flake, which can also be seen (b). (d) Stray field image of the tri-layer CrSBr flake at  $100\text{ K}$  determined from the pulsed ODMR signal. An outline of the flake based on co-registration with the PL image in (c) is shown by the grey dashed lines (Materials and Methods 1.6). (e) Simulation of the stray field projection from a single uncompensated FM layer of CrSBr onto the depth distribution of our NV ensemble (see Fig S9 for details). The grey dashed outline represents the position of the simulated CrSBr flake.



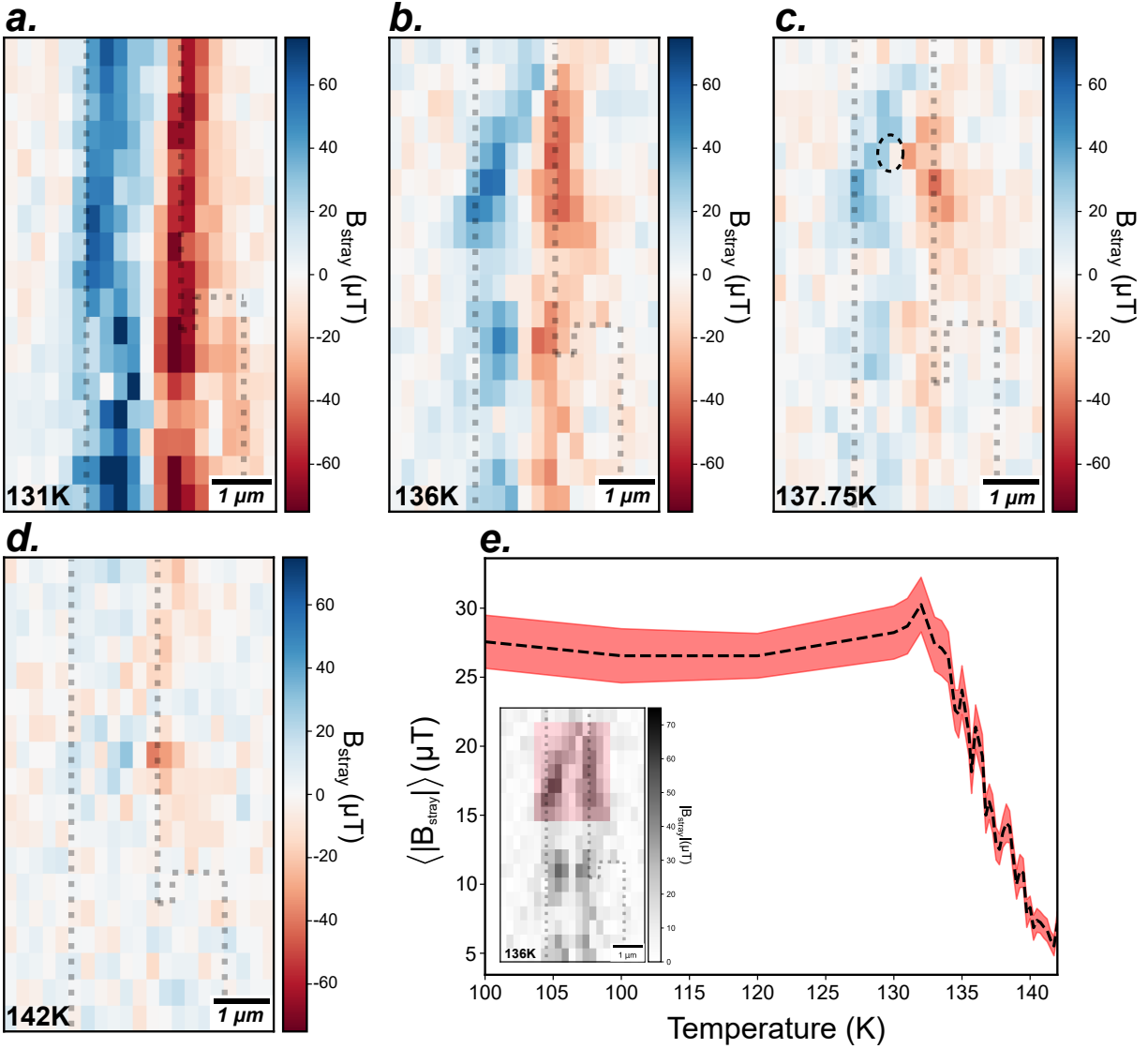


**Figure 2: Imaging the magnetic phase transition with DC magnetometry.** (a-d) Stray field images of tri-layer CrSBr from pulsed ODMR at temperatures across the magnetic phase transition. The gray dashed outlines represent the position of the CrSBr flake from co-registered CrSBr photoluminescence images. The black circle in (c) represents the location within the flake where spin echo measurements are performed (see Materials and Methods 1.6). (e)  $\langle |B_{stray}| \rangle$  as a function of temperature across the CrSBr phase transition, calculated from pixels in the highlighted region of the  $|B_{stray}|$  image in the inset. The width of the red shading on the  $\langle |B_{stray}| \rangle$  curve represents the standard deviation of the mean from pixels used to calculate  $\langle |B_{stray}| \rangle$ .

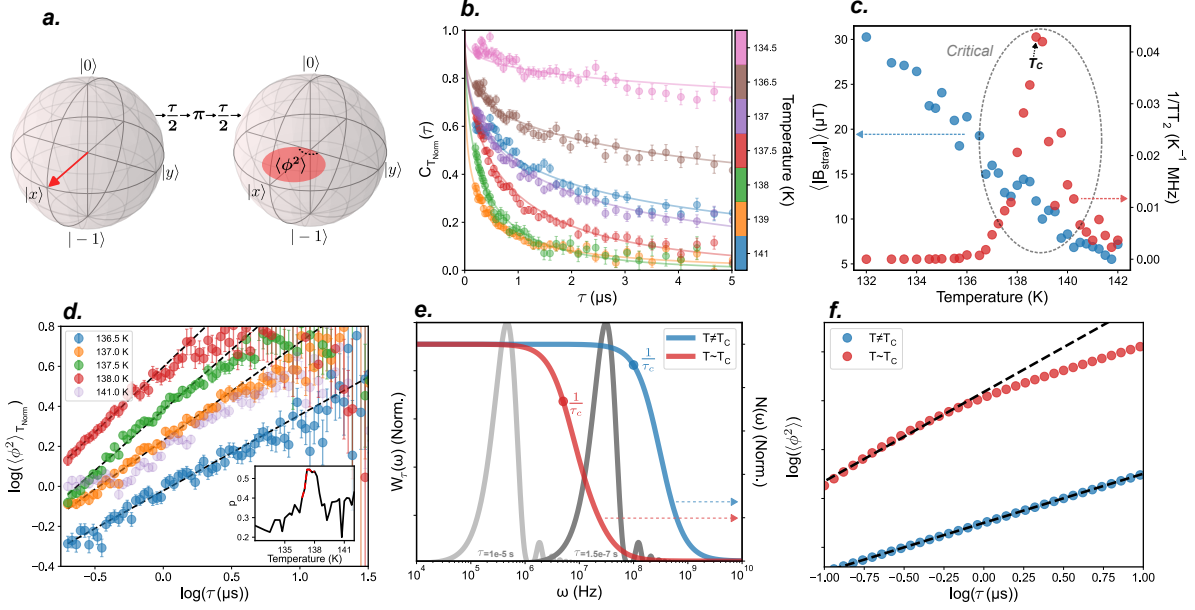


**Figure 3: Identifying critical fluctuations and critical slowing down of  $\tau_c$  from NV spin-decoherence.** (a) Bloch sphere representation of the evolution of  $\langle\phi^2(\tau)\rangle$  in the spin-echo experiment (note  $|x\rangle = (|0\rangle + |-1\rangle)/\sqrt{2}$  and  $|y\rangle = (|0\rangle + i|-1\rangle)/\sqrt{2}$ ). Note that  $\pi/2$  pulses from the full  $\pi/2(x) \rightarrow \tau/2 \rightarrow \pi(y) \rightarrow \tau/2 \rightarrow \pi/2(x,-x)$  spin-echo pulse sequence (Fig S6) are not shown. (b) Coherence decays  $C_{T_{Norm}}(\tau)$  (with  $T_{Ref} = 131$  K) for several representative temperatures across the CrSBr phase transition. Also shown are the corresponding stretched exponential fits evaluated from  $\tau = 0$  (solid lines). Based on our Rabi frequency (Fig S11), the shortest  $\tau$  that we select for measurements is 200 ns. (c) Comparison of  $\langle|B_{stray}|\rangle$  with  $1/TT_2$  across the CrSBr phase transition, with  $T_C$  identified from the  $1/TT_2$  peak at 138.75 K. The temperature range of critical fluctuations is  $\sim 136.5 - 141$  K. (d)  $\langle\phi^2(\tau)\rangle_{T_{Norm}}$  calculated from the data in (b) at selected temperatures in the range of critical fluctuations. Black dashed lines are linear fits to  $\log(\langle\phi^2(\tau)\rangle_{T_{Norm}})$  vs.  $\log(\tau)$ . The change in slope of the linear fits to  $\log(\langle\phi^2(\tau)\rangle_{T_{Norm}})$  vs.  $\log(\tau)$  as a function of temperature corresponds to a change in power law scaling of  $\langle\phi^2(\tau)\rangle_{T_{Norm}}$ , which is reflected by a peak in the temperature dependence of the stretch power  $p$  of the coherence decay  $C_{T_{Norm}}(\tau)$  (inset). The red trace in the inset highlights the temperature range of critical slowing down. (e) Simulations of the noise spectral density at temperatures away (blue) and near (red) criticality, with characteristic frequencies  $\omega_c = \tau_c^{-1}$  indicated. Also shown are spin echo filter functions  $W_\tau(\omega)$  for two values of  $\tau$  (10  $\mu$ s and 0.15  $\mu$ s) that approximately correspond to our experimental range. (f) Simulation of  $\langle\phi^2\rangle$  as a function of spin echo free evolution time  $\tau$  for the two different noise spectral density functions in (e), simulated over a range of  $\tau$  approximately spanning the limits of the filter functions shown in (e). We note that this range of  $\tau$  does not sample the high-frequency region of the noise spectrum at criticality that would result in asymptotic behavior in the early-time log-log scaling of  $\langle\phi^2(\tau)\rangle$  (23).

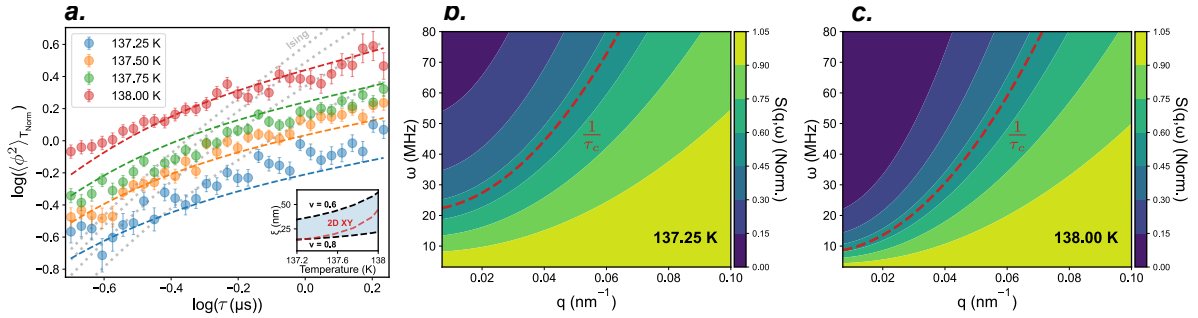


**Figure 4: Quantitative analysis of 2D critical dynamics.** (a). Data and mean-field simulation of  $\langle \phi^2(\tau) \rangle_{T_{Norm}}$  for temperatures in the window of critical slowing down, with  $T_{Ref} = 136.75$  K used for temperature normalization of the coherence decay (Eq (2) and Supplementary Text 2.2.1). The best fit parameters from the mean-field simulation are  $\nu = 0.73$ ,  $\omega_0 = 15.71$  GHz,  $J = 7.5$  meV (with  $T_C$  fixed at 138.75 K). Also shown is a simulation with  $\nu$  fixed to the value of  $\nu_{Ising} = 1$  (grey dashed curves, see Fig S13). (Inset) Range of temperature dependent behavior of the correlation length  $\xi$  for  $\nu = 0.6 - 0.8$  (indicated by the shaded blue region) compared with the behavior of  $\xi_{BKT}$ . A value of  $b = 0.28$  is used to evaluate  $\xi_{BKT}$  with the formula  $\xi_{BKT} = \xi_0 e^{b/\sqrt{(T-T_C)/T_C}}$  (44). (b), (c) Contour plots of the structure functions  $S(q, \omega)$  evaluated for two temperatures at criticality (137.25 K and 138 K, respectively) using the best fit parameters from the simulation in (a). The red dashed contour corresponds to the characteristic frequency  $\omega_c(q) = \tau_c(q)^{-1}$ , where  $\tau_c(q)$  is the fluctuation correlation time (see Supplementary Text 2.2.1). The shift of the  $\tau_c(q)^{-1}$  contour to lower frequencies between (b) and (c) illustrates critical slowing down of the fluctuation correlation time as temperature approaches  $T_C$ .

# Supplementary Materials for:

## Quantum Noise Spectroscopy of Criticality in an Atomically Thin Magnet

Mark E. Ziffer<sup>1,2,3\*</sup>, Francisco Machado<sup>4,5</sup>†, Benedikt Ursprung<sup>2</sup>†, Artur Lozovoi<sup>6,7</sup>†, Aya Batoul Tazi<sup>1</sup>†, Zhiyang Yuan<sup>6</sup>†, Michael E. Ziebel<sup>3</sup>, Tom Delord<sup>7</sup>, Nanyu Zeng<sup>8</sup>, Evan Telford<sup>3</sup>, Daniel G. Chica<sup>3</sup>, Dane W. deQuilettes<sup>9,10</sup>, Xiaoyang Zhu<sup>3</sup>, James C. Hone<sup>2</sup>, Kenneth L. Shepard<sup>8</sup>, Xavier Roy<sup>3</sup>, Nathalie P. de Leon<sup>6</sup>, Emily J. Davis<sup>11</sup>, Shubhayu Chatterjee<sup>12\*</sup>, Carlos A. Meriles<sup>7\*</sup>, Jonathan S. Owen<sup>3\*</sup>, P. James Schuck<sup>2\*</sup>, Abhay N. Pasupathy<sup>1,13\*</sup>

<sup>1</sup>Department of Physics, Columbia University, New York, NY 10027 USA

<sup>2</sup> Department of Mechanical Engineering, Columbia University, New York, NY 10027 USA

<sup>3</sup> Department of Chemistry, Columbia University, New York, NY 10027 USA

<sup>4</sup> ITAMP, Harvard-Smithsonian Center for Astrophysics, Cambridge, MA 02138, USA

<sup>5</sup> Department of Physics, Harvard University, Cambridge, MA 02138, USA

<sup>6</sup> Department of Electrical and Computer Engineering, Princeton University, Princeton, NJ 08540, USA

<sup>7</sup> Department of Physics, CUNY, The City College of New York, New York, NY, 10031, USA

<sup>8</sup> Department of Electrical Engineering, Columbia University, New York, NY 10027 USA

<sup>9</sup>Lincoln Laboratory, MIT, Lexington, MA, 02421, USA

<sup>10</sup>Center for Quantum Engineering, MIT, Cambridge, MA, 02139, USA

<sup>11</sup>Department of Physics, New York University, New York, NY 10003, USA

<sup>12</sup>Department of Physics, Carnegie Mellon University, Pittsburgh, PA 15213, USA

<sup>13</sup>Condensed Matter Physics and Materials Science Department, Brookhaven National Laboratory, Upton, NY, 11973 USA

†These authors contributed equally

\*Corresponding author. Email: apn2108@columbia.edu, p.j.schuck@columbia.edu, jso2115@columbia.edu, mz2733@columbia.edu, cmeriles@ccny.cuny.edu, shubhayuchatterjee@cmu.edu

# 1 Materials and Methods

## 1.1 NV Ensemble Preparation and Characterization

A [100]-oriented electronic grade diamond substrate with a  $\sim 2\mu m$  thick isotopically pure  $^{12}C$  overgrown diamond layer was purchased from QuantumDiamonds, GmbH. The as-received diamond was cleaned by ultrasonication followed by tri-acid cleaning in a boiling mixture of 1:1:1 perchloric:nitric:sulfuric acid refluxing for 2 hours. The  $^{12}C$  surface was then implanted with  $^{15}N^+$  ions with 25 keV implantation energy,  $2 \times 10^{12} cm^{-2}$  dose, and  $5^\circ$  sample tilt (Coherent, Inc., Innovion Corp., San Jose, CA). After ion implantation, the sample was cleaned with the tri-acid procedure and evaluated for surface contamination using XPS. The diamond was then annealed under vacuum ( $< 1 \times 10^{-5} Torr$ ) using the ramped annealing procedure reported by Sangtawesin *et al.* (51) without the  $1200^\circ C$  step, followed by tri-acid cleaning. The sample was then annealed under  $O_2$  gas at  $455^\circ C$  following the procedure in Sangtawesin *et al.* (51) in order to form an oxygen terminated surface to stabilize the  $NV^-$  charge state for NVs formed at shallow depths within the implanted  $^{15}N$  distribution (see Figure S1 for NV charge state characterization). Following  $O_2$  annealing the diamond was cleaned with a 1:2 hydrogen peroxide:sulfuric acid piranha solution. In between steps the diamond could be sonicated with Milli-Q water followed by sonication in electronic grade 2-propanol (Sigma Aldrich, 733458). The depth distribution of implanted  $^{15}N$  ions was determined from C-TRIM simulations as described below.

### 1.1.1 C-TRIM Depth Distribution Simulation

We modelled the  $^{15}N$  (and NV) depth distribution by performing C-TRIM (53, 54) simulations for 25keV  $^{15}N^+$  ion implantation into [100] oriented diamond. C-TRIM was used (as opposed to SRIM) to model the tail of the ion distribution at larger depths due to ion channelling (54). Based on the parameters determined by Raatz *et al.* (54) we used a value of  $C_{el} = 1.715$  for an implantation energy of 25keV. We additionally simulated surface roughness by adding a 3nm thick amorphous carbon layer with the density of diamond ( $3.51g/cm^3$ ) (54). Simulations were performed for a tilt angle of  $2^\circ$  to compensate for the  $\sim 3^\circ$  miscut angle of our diamond sample. Figure S2 shows the C-TRIM simulation results. The left axis (Figure S2) shows the

simulated  $^{15}N$  implantation density in ppm. We also fit the C-TRIM simulation to a sum of three truncated Gaussians, which was then normalized to an area of 1 to model an estimated probability density function  $P(d_{NV})$  for the NV depth  $d_{NV}$  (right axis, Figure S2). From the first moment of  $P(d_{NV})$  we determine a mean NV depth  $\langle d_{NV} \rangle = 46.6 \text{ nm}$ .

### 1.1.2 NV Ensemble Spin Coherence

To characterize the spin coherence properties of the NV ensemble we measured  $T_2$  using spin echo and  $T_2^*$  using Ramsey on a position  $\sim 1 \mu\text{m}$  off of the flake at  $\sim 137.5 \text{ K}$ . To compare the results with models for NV ensemble coherence, we first fit the spin echo coherence decay by numerically solving the ensemble averaged coherence model from Bauch *et al.* (55). Here, the coherence decay for a single NV undergoing decoherence from the diamond spin bath is defined as  $C(\tau) = e^{-\chi_{SE}(\tau)}$ , with  $\chi_{SE}(\tau) = \Delta_{single}^2 \tau_c^2 [\frac{\tau}{\tau_c} - 3 - e^{-\tau/\tau_c} + 4e^{-\tau/2\tau_c}]$  where  $\Delta_{single}^2$  determines the coupling strength to fluctuations from the diamond spin bath which have a characteristic fluctuation correlation time  $\tau_c$  (55). The coherence for an NV ensemble is obtained by solving  $C_{ens}(\tau) = \iint e^{-\chi_{SE}(\tau)} P(\Delta_{single}) P(\tau_c) d\Delta_{single} d\tau_c$  where  $P(\Delta_{single})$  is a probability distribution function for  $\Delta_{single}$  characterized by a shape parameter  $\Delta_{ens}$  and  $P(\tau_c)$  is a probability distribution for  $\tau_c$  with shape parameters  $\tau_{c,ens}$  and  $\lambda$  (55). Figure S3(a) shows the measured spin echo coherence  $C(\tau)$  and best fit to the model with  $\Delta_{ens} = 0.4 \text{ MHz}$ ,  $\tau_{c,ens} = 0.5 \mu\text{s}$ , and  $\lambda = 3.57$ . Defining  $C(\tau) = e^{-\langle \phi^2(\tau) \rangle / 2}$  as in the main text, we then evaluated the power law behavior of  $\langle \phi^2(\tau) \rangle$  from the model for  $C_{ens}(\tau)$  by plotting  $\langle \phi^2 \rangle$  vs  $\tau$  on a log-log scale (Figure S3(b)). Linear fitting of the early and late time log-log behavior of  $\langle \phi^2 \rangle$  vs  $\tau$  recovers the expected 3/2 and 1/2 power law behavior for  $\tau < \tau_{c,ens}$  and  $\tau > \tau_{c,ens}$  respectively for a 3D spin bath (Figure S3(b)) (23). To determine  $T_2$  we fit the coherence decay to a function  $C(\tau) = e^{-(\frac{\tau}{T_2})^{p(\tau)}}$  where we input a  $\tau$  dependent variation in the stretch parameter  $p(\tau)$  which is determined by calculating the derivative of  $\log(\langle \phi^2 \rangle)$  vs  $\log(\tau)$  from (Figure S3(b)). The calculated  $p(\tau)$  is shown in the inset of Figure S3(b). Figure S3(c) shows a fit of the data to  $e^{-(\frac{\tau}{T_2})^{p(\tau)}}$ , from which we determine  $T_2 = 13.2 \mu\text{s}$ . Based on the results of Bauch *et al.* (55) we would expect  $T_2$  in the range of 10's of  $\mu\text{s}$  for a bulk NV ensemble formed from 2.5 ppm nitrogen density. We suspect that due to the spread of NV depths near the surface in our ensemble (Fig S2) there is likely additional interaction between the NV ensemble and a surface

spin bath (with possible additional contributions of surface spin noise due residual polymer from the CrSBr transfer), which reduces  $T_2$ . We also measured  $T_2^*$  using a  $\frac{\pi}{2}(x) \rightarrow \frac{\pi}{2}(x,-x)$  Ramsey pulse sequence (see Figure S6 for pulse sequence). Figure S3(d) shows a fit of the Ramsey data to a function of the form  $C_{Ramsey}(\tau) \propto e^{-(\tau/T_2^*)} \cos(\omega_R \tau)$ , where  $\omega_R$  is the Ramsey interference frequency. From the fits to the Ramsey data we obtain  $T_2^* = 0.87 \mu s$ .

## 1.2 CrSBr Exfoliation and Transfer

Bulk crystals of CrSBr were synthesized using a chemical vapor transport reaction with a temperature gradient of  $950^\circ C$  to  $850^\circ C$  as described in detail in reference (29). Few-layer flakes of CrSBr were prepared by Scotch tape exfoliation from a bulk CrSBr crystal onto  $SiO_2(285 \text{ nm})/Si$  wafers. The thickness of the flakes were determined using atomic force microscopy and correlated optical contrast (27). Transfer of CrSBr flakes onto the diamond substrate was performed using a standard dry stamp method (56) with polycarbonate (PC) as the pick up polymer. The substrate was oriented on a rotation stage such that the long axis of the CrSBr flake of interest was aligned roughly parallel with a [110] edge of the diamond substrate as seen under the microscope camera prior to transfer. Following transfer the PC was washed off from the diamond with chloroform.

## 1.3 Confocal ODMR Setup

All experiments were performed on a home-built laser scanning confocal optically detected magnetic resonance (ODMR) microscope built around a Janis ST-500 optical cryostat (Figure S4). A 532 nm laser (Coherent Sapphire SF 532-50) is sent through an acousto-optic modulator (Isomet M1205-P80L-1) in a double-pass configuration for pulse modulation and directed via a 550 nm longpass dichroic mirror (Thorlabs DMLP550R) to a set of galvo-mirrors (Thorlabs GVS002) positioned in the back focal plane of the scan lens (Thorlabs SL50-CLS2) in a  $4f$  imaging system, where a tube lens (Thorlabs TTL200-S8) and a microscope objective (Nikon Plan Fluor 60x, 0.7NA) image the scanning laser spot onto the sample. Typical CW laser power on the sample is  $\sim 1 \text{ mW}$ . Photoluminescence (PL) from the sample is spectrally filtered with a 550 nm longpass dichroic mirror and additional 650 nm longpass filters, after which it is spatially filtered with  $30 \mu m$  pinhole. The PL is then split by a 850 nm dichroic mirror to separate

NV PL (in the range of 650-850 nm) from the CrSBr PL at  $\sim 930$  nm. The NV PL is sent to a fiber coupled single photon counting APD (Excelitas SPCM-AQRH-15-FC), and the CrSBr PL is sent to a superconducting nanowire single photon detector (Single Quantum EOS-6). Photon counts from the detectors are read out using gated counter channels on a DAQ (NI USB-6343). Microwave delivery was achieved by mounting the diamond onto a PCB resonator, where a  $\Omega$ -loop planar inductor delivered homogeneous RF magnetic fields over an area around  $\sim 0.5\text{mm}^2$  (see Figure S5 for details). The diamond was positioned on the PCB under a microscope such that the CrSBr flake was near the center of the  $\Omega$ -loop. The diamond was silver pasted onto the PCB and positioned such that it contacted cooling pads connected by vias to the ground plane of the PCB which is in thermal contact with the cold finger of the cryostat (see Figure S5). Microwaves are sourced from a signal generator (Stanford Research Systems SG384/3) and passed through a gated RF switch (MiniCircuits ZASWA-2-50DRA+) to generate pulses. Microwave pulses are then sent through an amplifier (MiniCircuits ZHL-16W-43-S+) and sent to the PCB. The output of the amplifier is protected with a circulator (DiTom D3C2040). Phase modulation of the microwave pulses is achieved by sending input signals (generated by gating a DC voltage with MiniCircuits ZASWA-2-50DRA+ switches) to the IQ modulator built into the SG384/3 (57). A PulseBlaster ESR-Pro-500 pulse generator is programmed to deliver TTL pulses through output channels to control modulation of the AOM, gating of microwave switches, and gating of DAQ counter channels (see Section 2.2 and Figure S6). Two 3" OD ring magnets (K&J Magnetics RZ0Y0X0) are mounted in a coaxial configuration outside the cryostat on a 5-axis stage and are adjusted such that a  $\sim 3.5\text{ mT}$  bias field is aligned along a [111] axis of the diamond (see Section 2.3 and Figure S7). The cryostat is cooled with a closed cycle Helium recirculating system (Janis RGC4) and the temperature is maintained using a PID temperature controller (Lakeshore 335). All instruments and experiments are controlled using custom written Python code with the ScopeFoundry platform (58).

## 1.4 Pulse Sequences and Contrast Definitions

The detailed pulse sequences for pulsed ODMR, spin echo, Rabi, Ramsey, and CW ODMR experiments are shown in Figure S6. For pulsed ODMR, Rabi and CW ODMR experiments, the raw contrast is defined as  $\frac{\text{Signal}-\text{Reference}}{\text{Reference}}$  (“signal” and “reference” corresponding to data



from the readout channels of the DAQ). For spin echo (or Ramsey) experiments raw contrast is defined as  $2\frac{Signal-Reference}{Signal+Reference}$  (57).

## 1.5 Magnetometry

For all AC and DC magnetometry measurements the bias magnetic field is aligned such that the B-field direction is projected along one of the four possible [111] directions of diamond, corresponding to the spin quantization axis of one of four possible subsets of NV orientations in the ensemble (57). Figure S7(a) shows the CW ODMR spectrum representing a typical magnetic field alignment. The field is aligned so that the ODMR spectra for the three “off axis” NV orientations (orientations which have the the magnetic field projected partially off-axis from the spin quantization axis) collapse onto one peak with the  $\sim 3\text{ MHz }^{15}\text{N}$  hyperfine splitting (61) overlapped when measured with low microwave power (inset of Fig S7(a)). Rabi measurements (see Figure S11(d)) are then performed at the  $|m_s = 0\rangle \rightarrow |m_s = -1\rangle$  resonance frequency for the “on axis” NV orientation to determine the  $\pi$ - pulse duration for all subsequent coherent pulsed experiments . For pulsed ODMR imaging experiments, seven frequency points are measured which correspond to zero-crossings of 1st, 2nd, 3rd and 4th derivatives of a Lorentzian fit determined from a spectrum initially measured at a position  $\sim 1\mu\text{m}$  away from the flake (Figure S7(b)). These seven points correspond to the main points of curvature of a Lorentzian function which allows us to fit the pulsed ODMR data measured at each pixel to a full Lorentzian function to create images both of the resonance frequency and pulsed ODMR contrast (see Section 3).

## 1.6 Sample Drift Correction

In pulsed ODMR imaging experiments, the average count rate from the SNSPD (which records PL from CrSBr) is recorded at each pixel along with the data from the pulsed ODMR pulse sequence (Figure S6), such that PL images of the CrSBr flake and pulsed ODMR images can be constructed from data recorded simultaneously. Typically 460 pixels are recorded for each image with 5000 pulsed ODMR averages per pixel (averaging  $1.6\text{ s/pixel}$  and a total of  $\sim 12\text{ min/image}$ ), and  $> 20$  images are recorded which amounts to a total of  $> 1e5$  pulsed ODMR averages per pixel. Over the course of a several hour measurement, the image will

drift slowly (over 10's of minutes) on the scale of 100's of nm to  $\sim \mu m$ , which is found to be correlated with thermal fluctuations in the room and is likely due to thermal drift of the optics. This drift is corrected in image post processing by cross correlating the first CrSBr PL image recorded in the measurement sequence with each image in subsequent sequences. The drift is calculated with sub-pixel accuracy using the SCIKIT-IMAGE phase cross correlation routine (62) and is determined as a function of time using the image file timestamps. Image interpolation is then used to correct pixel assignments for images recorded at different times in the measurement and reconstruct drift corrected PL and pulsed ODMR images.

For spin echo experiments drift correction is performed on the fly so that a fixed measurement position on the sample is maintained over long measurement periods. An initial PL image of the CrSBr flake is recorded and position coordinates on the PL image to perform spin echo measurements are selected. A series of spin echo pulse sequences (typically  $1e5$ ) for 75 different interpulse delay times ( $\frac{\tau}{2}$ ) are then performed at the given coordinates which takes  $\sim 6 - 7 min$ . Another PL image is then measured and cross-correlated with the initial PL image to determine the sample drift and the target coordinates for the next series of spin echo measurements are updated to correct for drift. The process is repeated 75 – 100 times for a total of  $1e6 - 1e7$  averages of the spin echo pulse sequence. The typical spread of coordinates sampled over the total course of spin echo measurements (with variation due to differences in the results of image cross correlation) is shown by the red dots in Figure S8.

## 2 Supplementary Text

### 2.1 Temperature Range of Spin Echo Normalization

At temperatures near the CrSBr phase transition, we observed a decrease in the pulsed ODMR contrast in the interior region of the CrSBr flake relative to the contrast outside the flake (Figure S10a). This effect is consistent with the formation of sub-diffraction-limited static magnetic domains in the flake interior near the  $T_C$  as reported in few-layer CrSBr by Tschudin *et al.* with scanning NV magnetometry (31), which we would expect to broaden the inhomogeneous linewidth ( $\Gamma$ ) of the NV ensemble probed by the diffraction-limited laser spot in our experiment. Changes in the ratio of the Rabi frequency  $\Omega$  to the inhomogeneous linewidth  $\Gamma$  with temperature could affect the signal contrast in spin echo experiments (64), complicating the comparison of data across a broad temperature range.

In the following analysis we show that, based on the variation in pulsed ODMR contrast in the temperature range of  $\sim 130 - 140K$ , we do not expect spin echo contrast to vary significantly enough to affect the analysis of the decoherence dynamics discussed in the main text. In particular, we show that the measured pulsed ODMR contrast (Figure S10a) can be used as a proxy to determine the ratio  $\Omega/\Gamma$  at all temperatures. We then perform numerics to simulate the spin echo protocol at each value of  $\Omega/\Gamma$  and demonstrate that the maximum effect on the normalized spin echo contrast is negligible.

We begin by comparing the pulsed ODMR contrast in the interior and exterior regions of the flake as a function of temperature. Since the Rabi frequency  $\Omega$  is fixed across all measurements, this comparison will allow us to evaluate temperature-dependent changes in the inhomogeneous broadening  $\Gamma$  within the flake to the (temperature-independent) reference value outside the flake  $\Gamma_0$ . We use our drift correction method (Section 2.4) to track the spread of spatial points sampled over the total course of spin echo measurements at  $137.5 K$ , which is shown by the red dots overlaid on the pulsed ODMR contrast image in Figure S10a. From the spread of points we determine the probability that a pixel in the image was sampled during the spin echo measurement (Figure S10b) and calculate an average pulsed ODMR contrast for those points, obtained at  $\Omega/\Gamma$ . We also calculate an average pulsed ODMR contrast for a region of pixels off of the flake obtained at  $\Omega/\Gamma_0$  (Figure 10c) and determine the ratio of on-flake/off-flake pulsed

ODMR contrast. This process is repeated for the data taken at all temperatures and the ratio of on-flake/off-flake pulsed ODMR contrast as a function of temperature is shown in Figure S10d.

Next, we demonstrate that the ODMR contrast ratio plotted in Figure S10d is a valid proxy for the ratio  $\Gamma/\Gamma_0$ . We begin by simulating the Rabi contrast for an inhomogeneously broadened NV ensemble. We model the two-level dynamics of the pseudo-spin-1/2 subspace of the NV ground state (65, 66) using QISKIT DYNAMICS (67), where we define a rotating frame Hamiltonian in the  $S_z$  basis with eigenstates  $|\alpha\rangle = \begin{pmatrix} 1 \\ 0 \end{pmatrix}$  and  $|\beta\rangle = \begin{pmatrix} 0 \\ 1 \end{pmatrix}$ :

$$H = h_z s_z + h_x s_x \quad (\text{S1})$$

where  $s_z$  and  $s_x$  are the Pauli spin-1/2 operators,  $h_x = 2\pi\Omega$  (where  $\Omega$  is the Rabi frequency), and  $h_z$  is the off-resonance Zeeman energy. In each simulation the initial state is set to  $|\psi_0\rangle = |\alpha\rangle$  and the state is evolved over time (in units of  $t_{2\pi} = 1/\Omega$ ). To simulate Rabi oscillations for different ratios of  $\Omega/\Gamma$ , we set the Rabi frequency  $\Omega = 1$  for all simulations and randomly select values of  $h_x$  from a normal distribution of width  $2\pi\Gamma$ . For a given normal distribution, we simulate the dynamics for  $> 10^3$  values of  $h_z$ , calculating the expectation value  $\langle S_z \rangle = \frac{1}{2}(|c_\alpha|^2 - |c_\beta|^2)$  at each time point for each value of  $h_z$ . We then average the results over all values of  $h_z$  to compute the ensemble averaged expectation value  $\langle S_z \rangle_{ens}$ , and take  $\frac{1}{2} + \langle S_z \rangle_{ens}$  as the simulated contrast (65). Simulations are performed for a range of  $\Gamma$  from 0.1 – 10. Figure S11a shows the simulated Rabi oscillations for two values of  $\Omega/\Gamma$ , which are fit to a function of the form:

$$Ae^{-t/T_{\text{Rabi}}} \cos(2\pi\Omega t) + B \quad (\text{S2})$$

where  $T_{\text{Rabi}}$  is a time constant for the Rabi decay. Figure S11b shows  $T_{\text{Rabi}}$  (in units of  $t_{2\pi}$ ) determined for a wide range of  $\Omega/\Gamma$ . Figures S11c,d show the Rabi oscillations measured at on-flake and off-flake positions at 137.5K. By fitting the data in Figures S11c,d we extract a decay time  $T_{\text{Rabi}}$  in units of  $t_{2\pi}$ , from which we can determine values of  $\Omega/\Gamma$  by interpolating Figure S11b. We determine a value of  $\Omega/\Gamma_0 = 3.1$  for the off-flake position and  $\Omega/\Gamma = 1.03$  for the on-flake position at 137.5K. Next we determine the contrast for a  $\pi$ -pulse by evaluating  $\frac{1}{2} + \langle S_z \rangle_{ens}$  at  $t = 0.5$  from the Rabi oscillation simulations. Figure S11e shows the simulated  $\pi$ -pulse contrast as a function of  $\Omega/\Gamma$ . Using the on-flake  $\Omega/\Gamma$  and off-flake  $\Omega/\Gamma_0$  values at 137.5K determined above, we use Figure S11e to estimate the value for the ratio of on-

flake/off-flake  $\pi$ -pulse ODMR contrast. We determine an estimated value of 0.58, which is in good agreement with the experimental value of 0.64 at 137.5K (Figure S10d). Assuming that the off-flake  $\Omega/\Gamma_0 = 3.1$  is temperature independent, we then use the ratios of measured on-flake/off-flake pulsed ODMR contrast from Figure S10d to determine the values of the on-flake  $\Omega/\Gamma$  ratio at all temperatures (Figure S11f).

In order to understand the effect of the trend in Figure S10d on spin echo measurements, we determine an approximate relationship between the on-flake/off-flake pulsed ODMR contrast and initial spin contrast by performing a master equation simulation of spin echo as a function of  $\Omega/\Gamma$ . We define a time-dependent Hamiltonian to simulate coherent driving in a spin echo  $\frac{\pi}{2}(x) \rightarrow \pi(y) \rightarrow \frac{\pi}{2}(x,-x)$  pulse sequence with zero interpulse delay:

$$H = h_z s_z + H_1(t) \quad (\text{S3})$$

$$H_1(t) = 2\pi\Omega \begin{cases} s_x & 0 \leq t \leq \frac{1}{4} \\ s_y & \frac{1}{4} \leq t \leq \frac{3}{4} \\ s_{x,-x} & \frac{3}{4} \leq t \leq 1 \end{cases}$$

Here two simulations are performed: one with a final  $s_x$  rotation and one with a final  $s_{-x}$  rotation. Using a similar method to model inhomogeneous broadening as described above, we fix  $\Omega = 1$  and perform simulations over randomly selected values of  $h_z$  taken from a normal distribution of width  $2\pi\Gamma$ , and evaluate the results for different values of  $\Gamma$ . In each simulation the initial spin echo contrast is defined as  $\langle S_z \rangle_{echo} = \langle S_z \rangle_x - \langle S_z \rangle_{-x}$ , evaluated at  $t = 1$  (in units of  $t_{2\pi}$ ). For each value of  $\Gamma$  we average the contrast for all values of  $h_z$  to determine the ensemble averaged spin echo contrast  $\langle S_z \rangle_{ens_{echo}} = \langle S_z \rangle_{ens_x} - \langle S_z \rangle_{ens_{-x}}$ . Figure S12a shows the simulated initial spin echo contrast as a function of  $\Omega/\Gamma$ . Using the temperature-dependent values of the on-flake  $\Omega/\Gamma$  determined above (Figure S11f), we interpolate Figure S12a to estimate the fraction of spin echo contrast lost at each temperature in our experiment (Figure S12b), which shows that there is not a strong trend of spin echo contrast loss with temperature in the range of 130 – 142K. We quantify the spread of spin echo contrast loss in the range of 130 – 142K with a histogram (Figure S12c) which shows a variation of around 5% relative change the mean value of contrast loss (0.68).

To understand how this variation in spin echo contrast loss could impact the data, we compared two sets of temperature-normalized spin echo coherence decays  $C_{T_{Norm}}(\tau)$ : one with the

raw data at all temperatures normalized relative to the raw data at  $T_{Norm} = 131K$ , and one with raw the data at each temperature scaled by a relative correction factor prior to normalization based on the estimated temperature dependent contrast loss from Figure S12b. Figures S12d,e show that there is little difference in the temperature normalized data with or without a correction for contrast loss. We also fit both the corrected and uncorrected data sets to stretched exponential functions and compare the temperature dependence of the extracted  $\frac{1}{TT_2}$  rates and stretch parameters  $p$ . Figures S12f,g show that the trends in  $\frac{1}{TT_2}$  and  $p$  observed at criticality are nearly identical with or without a contrast correction, indicating that our analysis of the spin echo dynamics at criticality is not likely to be impacted by changes in spin echo contrast.

Finally, we verify that the effect of the  $\Omega/\Gamma$  ratio on spin manipulation does not affect the observed decoherence dynamics by simulating a  $\frac{\pi}{2}(x) \rightarrow \tau \rightarrow \pi(y) \rightarrow \tau \rightarrow \frac{\pi}{2}(x,-x)$  spin echo sequence with pure dephasing and variable interpulse delay  $\tau$ . Here we define a Hamiltonian:

$$H = h_z s_z + H_1(t) \quad (\text{S4})$$

$$H_1(t) = 2\pi\Omega \begin{cases} s_x & 0 \leq t \leq \frac{1}{4} \\ s_y & \tau + \frac{1}{4} \leq t \leq \tau + \frac{3}{4} \\ s_{x,-x} & 2\tau + \frac{3}{4} \leq t \leq 2\tau + 1 \end{cases}$$

with  $t$  and  $\tau$  in units of  $t_{2\pi}$ . To simulate pure dephasing we define a relaxation operator  $\sqrt{\Gamma_2} s_z$  for the dissipative term of the Lindblad equation which causes the off-diagonal elements of the density matrix to decay at a rate  $2\Gamma_2$ . Simulations for a range of  $\Omega/\Gamma$  are performed in the same way as above for the initial spin echo contrast, with  $\Omega = 1$  and  $\Gamma_2 = 0.3$  fixed for all simulations. Figure S12h shows the results of simulations for three different values of  $\Omega/\Gamma$ . Figure S12i shows the simulations normalized to the value of  $\langle S_z \rangle_{echo}$  at  $\tau = 0$ , which shows that the measured decoherence dynamics in the  $\frac{\pi}{2}(x) \rightarrow \tau \rightarrow \pi(y) \rightarrow \tau \rightarrow \frac{\pi}{2}(x,-x)$  spin echo pulse sequence are not changed by the effect of  $\Omega/\Gamma$  on spin manipulation.

## 2.2 Critical Dynamics Analysis

### 2.2.1 Simulation Methods and Definitions

We simulated the ensemble decoherence from the mean-field derived structure functions following the derivations from Machado *et al.* (15). We start with the calculation of  $\langle \phi^2 \rangle$  for a

single NV center at a depth  $d$  from the 2D flake, given by:

$$\langle \phi^2 \rangle = \int_{\omega_L}^{\omega_U} W_\tau(\omega) \frac{d\omega}{2\pi} \int_0^{1/a} W_d(q) S(q, \omega) \frac{dq}{2\pi} \quad (\text{S5})$$

with:

$$W_\tau(\omega) = \left( \frac{2g_e\mu_b}{\hbar} \right)^2 \frac{\sin\left(\frac{\omega\tau}{4}\right)^4}{\omega^2} \quad (\text{S6})$$

where  $g_e$  is the electron g-factor and  $\mu_B$  is the Bohr magneton, and:

$$W_d(q) = \frac{(\mu_0\mu_B g_e S)^2}{4a^4} q^3 e^{-2qd} \quad (\text{S7})$$

where  $\mu_0$  is the vacuum permittivity,  $S = \frac{3}{2}$  is the electron spin for  $Cr^{3+}$  (25), and  $a = 4.7485 \text{ \AA}$  is taken as the CrSBr lattice constant (26). The limits on the first integral in (5) are set by the approximate width of the spin echo filter function  $\omega_L = \frac{\pi-1}{\tau}$  and  $\omega_U = \frac{\pi+1}{\tau}$  (15). Restating from the main text we have:

$$S(q, \omega) = \frac{2k_B T \Gamma_0}{\Gamma_0^2 J^2 (\xi^{-2} + q^2)^2 + \omega^2} \quad (\text{S8})$$

where  $J$  is the exchange energy and  $\Gamma_0$  is the kinetic coefficient defined as  $\Gamma_0 = \frac{\omega_0}{J\xi_0^2}$  where  $\omega_0$  is a low temperature characteristic fluctuation frequency which can be compared with low temperature magnon frequencies reported in the literature (39) and  $\xi_0$  is a low temperature fluctuation correlation length taken as  $2a$  (15). The temperature dependent correlation length  $\xi$  is defined as:

$$\xi = \xi_0 \left| \frac{T - T_C}{T_C} \right|^{-\nu} \quad (\text{S9})$$

where  $T_C$  is the critical temperature and  $\nu$  is the critical exponent for the fluctuation correlation length. From the structure function (8) we also define the characteristic frequency  $\omega_c(q)$  (15):

$$\omega_c(q) = \Gamma_0 J (\xi^{-2} + q^{-2}) \quad (\text{S10})$$

where  $\omega_c(q)$  is related to the fluctuation correlation time  $\tau_c$  by  $\omega_c(q) = \tau_c(q)^{-1}$  which is used to determine  $\tau_c(q)^{-1}$  in Figures 4b,c of the main text. The coherence for a single NV is defined as:

$$C(\tau) = e^{-\frac{1}{2}\langle \phi^2 \rangle} \quad (\text{S11})$$

To model an ensemble averaged coherence, we calculate the expectation value for  $C(\tau)$  over the probability distribution function for the NV depth ( $P(d_{NV})$ ) determined from the C-TRIM simulation (Figure S2):

$$C^{ens} = \int e^{-\frac{1}{2}\langle\phi^2\rangle_{d_{NV}}} P(d_{NV}) dd_{NV} \quad (S12)$$

The depth dependence of  $\langle\phi^2\rangle$  comes in via (7) and is indicated explicitly by the notation  $\langle\phi^2\rangle_{d_{NV}}$ . We perform simulations for 51 different NV depths  $d_{NV}$  spanning the range covered by  $P(d_{NV})$  in Figure S2 and numerically calculate  $C^{ens}$  from (12). The ensemble averaged variance of the stochastic phase  $\langle\phi^2\rangle^{ens}$  is then defined as:

$$\langle\phi^2\rangle^{ens} = -2\ln(C^{ens}) \quad (S13)$$

We calculate the temperature normalized coherence  $C_{T_{Norm}}^{ens}$  and variance of the stochastic phase  $\langle\phi^2\rangle_{T_{Norm}}^{ens}$  as:

$$C_{T_{Norm}}^{ens} = \frac{C_T^{ens}}{C_{T_{Ref}}^{ens}} \quad (S14)$$

$$\langle\phi^2\rangle_{T_{Norm}}^{ens} = -2\ln(C_{T_{Norm}}^{ens}) \quad (S15)$$

which we use for the fits in Figure 4a of the main text.

The numerical integration of (5) is time consuming to the extent that it is unfeasible to use gradient optimization routines and a cost function to vary parameters  $J$ ,  $\omega_0$  and  $\nu$  over a range of  $d$  for determining best fit models of  $\langle\phi^2\rangle_{T_{Norm}}^{ens}$  to the data. Instead, we build a library of simulations for  $\langle\phi^2\rangle_{T_{Norm}}^{ens}$  over ranges of parameter values for  $J$ ,  $\omega_0$  and  $\nu$ . We then determine the best fit by selecting the parameter values that give the minimum of a global  $\chi_{tot}^2$  metric that evaluates the overall goodness-of-fit to the global set of temperature dependent data, which is defined as  $\chi_{tot}^2 = \sqrt{(\chi_{T_1}^2)^2 + (\chi_{T_2}^2)^2 + \dots + (\chi_{T_N}^2)^2}$  where  $\chi_{T_N}^2$  is the  $\chi^2$  value for the data at temperature  $T_N$ . As described in the main text, we fit the  $\langle\phi^2\rangle_{T_{Norm}}^{ens}$  data using a set of four temperatures 137.25 K, 137.5 K, 137.75 K, 138 K where we expect to see mean-field predicted critical slowing down based on the trend of the stretch power from stretched exponential fits to the decoherence (main text, Figure 3d inset).



### 2.2.2 Effects of the NV Ensemble Depth Distribution on Decoherence Dynamics

In this section, we perform a simple calculation demonstrating how the observed stretch-power is controlled by the NV depth distribution in an ensemble sample. In general, the precise functional form depends on many details of the coherence dynamics, but a simple estimation can illustrate how different NV density distributions lead to different stretch exponents. To this end, let us assume that at a depth  $z$ , the NV coherence dynamics is given by a stretched exponential form:

$$C(z, t) = e^{-\lambda_0 t^p / z^a}$$

where  $\lambda_0$  captures the overall coupling strength,  $1/z^a$  captures the depth dependence of the coupling between the NV and the sample. The overall coherence can be estimated as follows: the NV remains coherent until  $\lambda_0 t^p / z^a \gtrsim 1$ . This implies that, at time  $t$ , the coherence signal is approximated by the fraction of NVs that are located at a depth  $z > z^* = (\lambda_0 t^p)^{1/a}$ . The resulting functional form is:

$$C_{\text{tot}}(t) \approx \int_{z^*}^{\infty} dz \rho(z) \quad (\text{S16})$$

Assuming a generic functional form  $\rho(z) \propto z^{k_1} e^{-(z/\xi)^{k_2}}$ , we can analyze the time dependence of the signal:

$$C_{\text{tot}}(t) \propto \int_{(\lambda_0 t^p)^{1/a}}^{\infty} dz z^{k_1} e^{-(z/\xi)^{k_2}} = \xi^{k_1+1} \int_{(\lambda_0 t^p)^{1/a}/\xi}^{\infty} dy y^{k_1} e^{-y^{k_2}} = \xi^{k_1+1} \frac{\Gamma_{\frac{1+k_1}{k_2}}(y_0^{k_2})}{k_2} \Bigg|_{y_0=(\lambda_0 t^p)^{1/a}/\xi} \quad (\text{S17})$$

$$\xrightarrow{t \rightarrow \infty} C_0 \exp \left[ - \underbrace{t^{pk_2/a}}_{\text{stretch power}} \lambda_0^{k_2/a} \xi^{-k_2} \right] t^{(-k_2+1+k_1)p/a} \quad (\text{S18})$$

where  $C_0$  is a normalization factor that depends on  $\lambda_0$  and  $\xi$ , and the polynomial terms in Eq. (S18) would manifest in a log-correction to the observed stretch-power. While a simple estimation, this calculation immediately highlights, for an ensemble sample, that the observed stretch exponent depends not only on the stretch exponent for a single NV (which is  $p$ ), but also on how the NV couples to the sample (captured here by  $a$ ) as well as the tail distribution of the NV depth (encoded in  $k_2$ ).

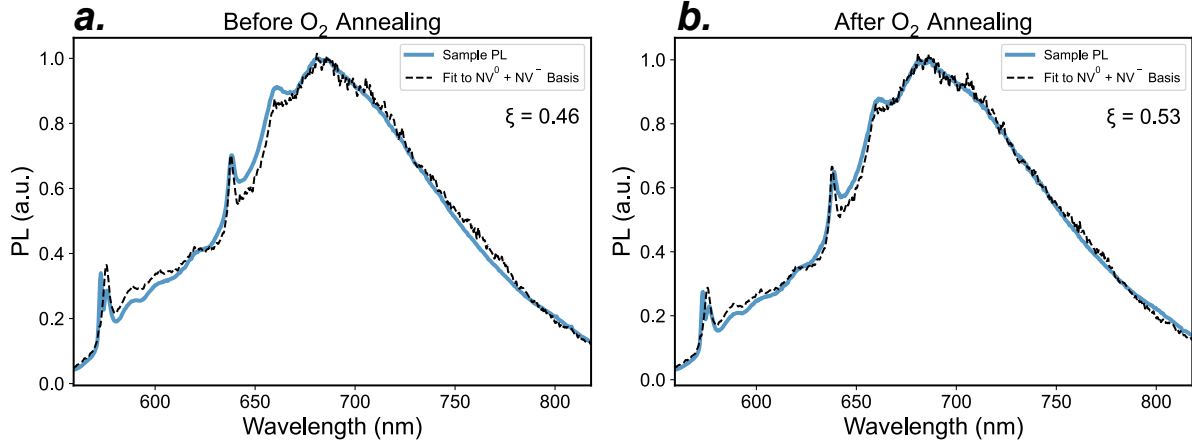


**Figure S1: Photoluminescence characterization of the NV ensemble charge state ratio.** We determined the  $NV^-$  to  $NV^0$  ratio before and after the  $O_2$  annealing steps of our sample preparation using the photoluminescence decomposition method of Alsid *et al.* (52). Photoluminescence spectra were measured on a confocal fluorescence set up using  $\sim 1.8mW$  532 nm CW laser excitation focused onto the sample with a 0.6 NA objective (Olympus LUCPlanFL N, 40x). Dichroic and longpass filters were used to filter the laser excitation and the fluorescence spectra were recorded with a spectrograph (Acton SP2300i) and CCD camera (Princeton Instruments Pixis 400BRX). The data were intensity corrected by measuring the spectrum of a calibrated tungsten halogen light source (StellarNet SL1-CAL). The fraction of the total NV yield in the  $NV^-$  charge state ( $\xi$ ) was determined by fitting the spectra to a sum of basis functions  $c_-$  and  $c_0$  (corresponding to the emission spectra of  $NV^-$  and  $NV^0$ , respectively), and weighting  $c_0$  by a factor  $\kappa_{532}$  corresponding to the difference in emission rate between the  $NV^-$  and  $NV^0$  charge states excited at 532 nm, using the equation:  $\xi = \frac{[NV^-]}{[NV^-]+[NV^0]} = \frac{c_-}{c_- + \kappa_{532}c_0}$  (52).  $O_2$  annealing was found to improve the total  $NV^-$  fraction by a factor of  $\sim 15\%$  ( $\xi = 0.46$  before  $O_2$  annealing to  $\xi = 0.53$  after  $O_2$  annealing).

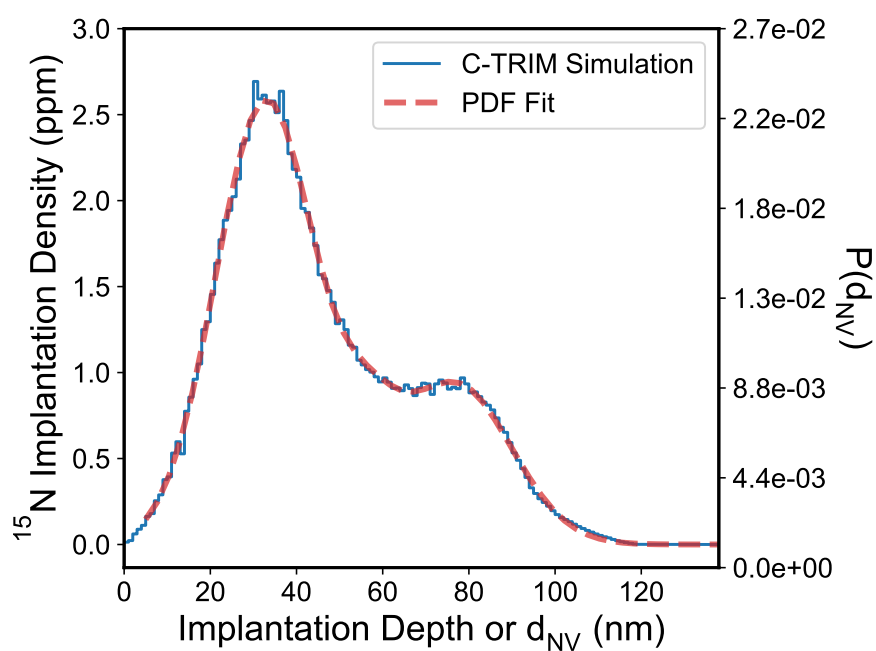


**Figure S2: C-TRIM  $^{15}N$  ion implantation simulation.** (Left axis) C-TRIM simulation of the  $^{15}N$  implantation density as a function of depth (see Section 1.1.1 for simulation details). (Right axis) Probability density for the  $^{15}N$  (and NV) depth based on fits to the C-TRIM depth distribution (see Section 1.1.1 for details).

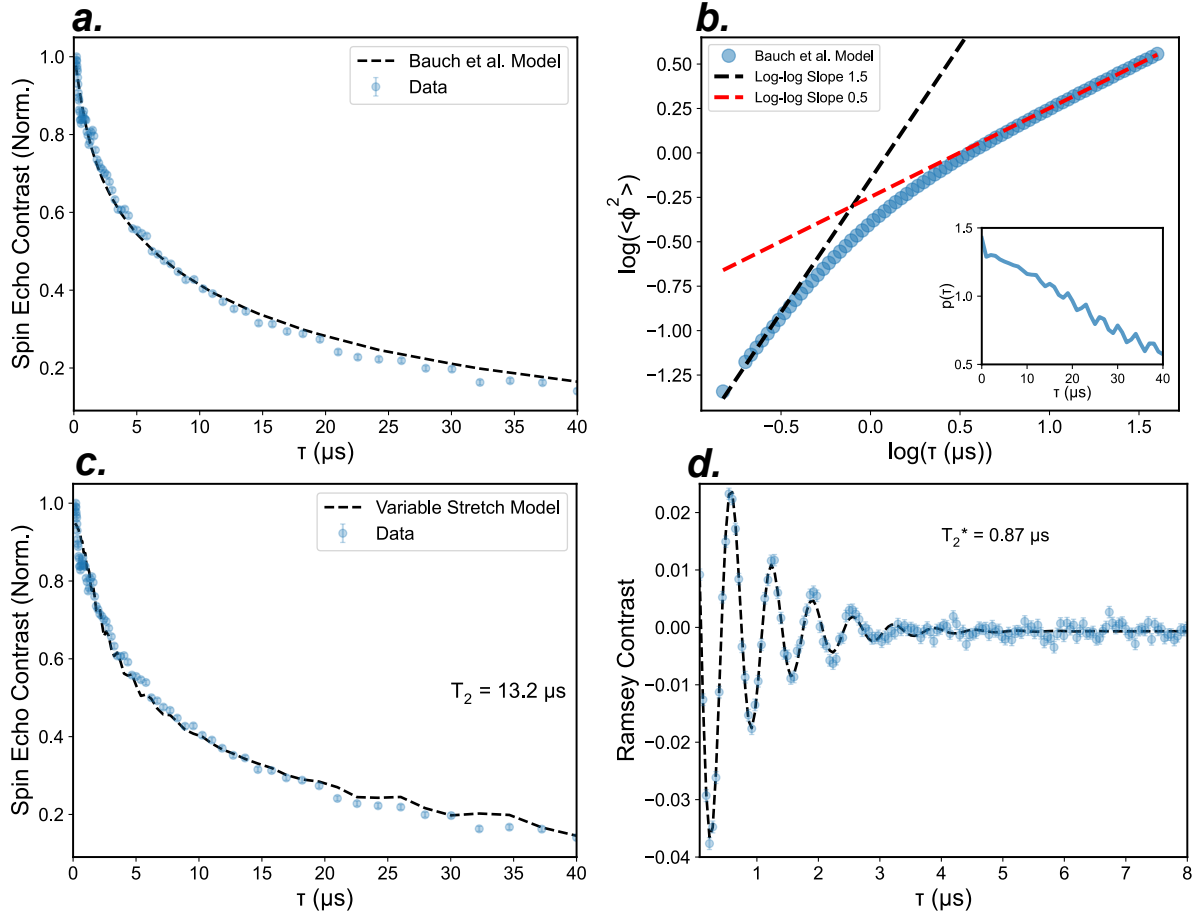


**Figure S3: Spin coherence of the NV ensemble.** (a) Spin echo coherence decay of the NV ensemble at 137.5 K fit to the model of Bauch *et al.* (55) for ensemble averaged NV interactions with the bulk diamond spin bath (see Section 1.1.2). (b) Power law scaling of  $\langle \phi(\tau)^2 \rangle$  determined by linear fits to  $\log(\langle \phi(\tau)^2 \rangle)$  vs  $\log(\tau)$  derived from the model in (a). Inset shows the  $\tau$  dependence of the exponential stretch parameter  $p(\tau)$  of the coherence decay, determined by calculating  $d\log(\langle \phi(\tau)^2 \rangle)/d\tau$ . (c) Fit of the data in (a) to  $e^{-(\frac{\tau}{T_2})^{p(\tau)}}$  using  $p(\tau)$  determined in (b). (d) Free induction decay of the NV ensemble measured by a Ramsey pulse sequence at 137.5 K (see Figure S6).

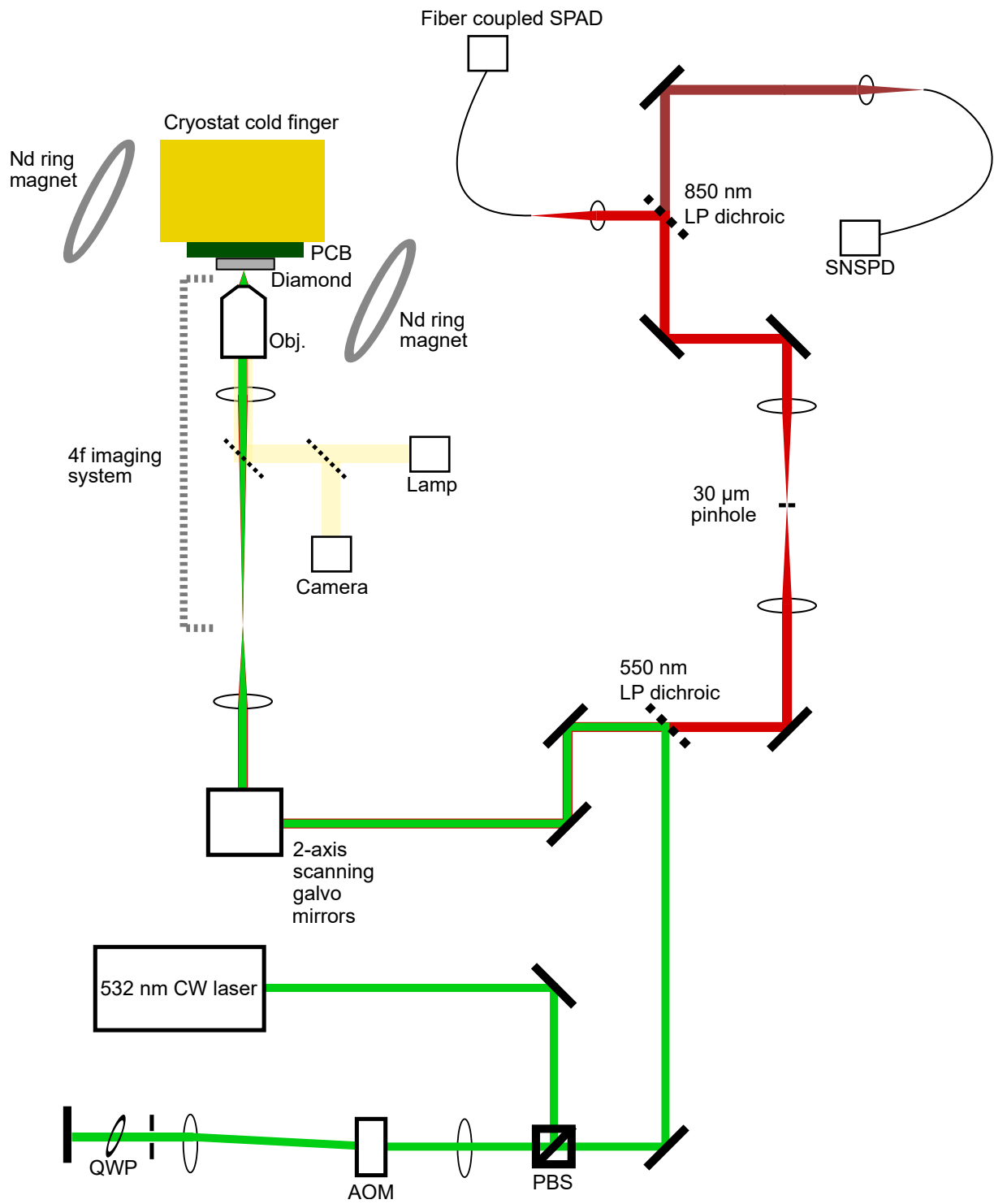


**Figure S4: Experimental set-up.** Diagram of the confocal ODMR setup used in this work.

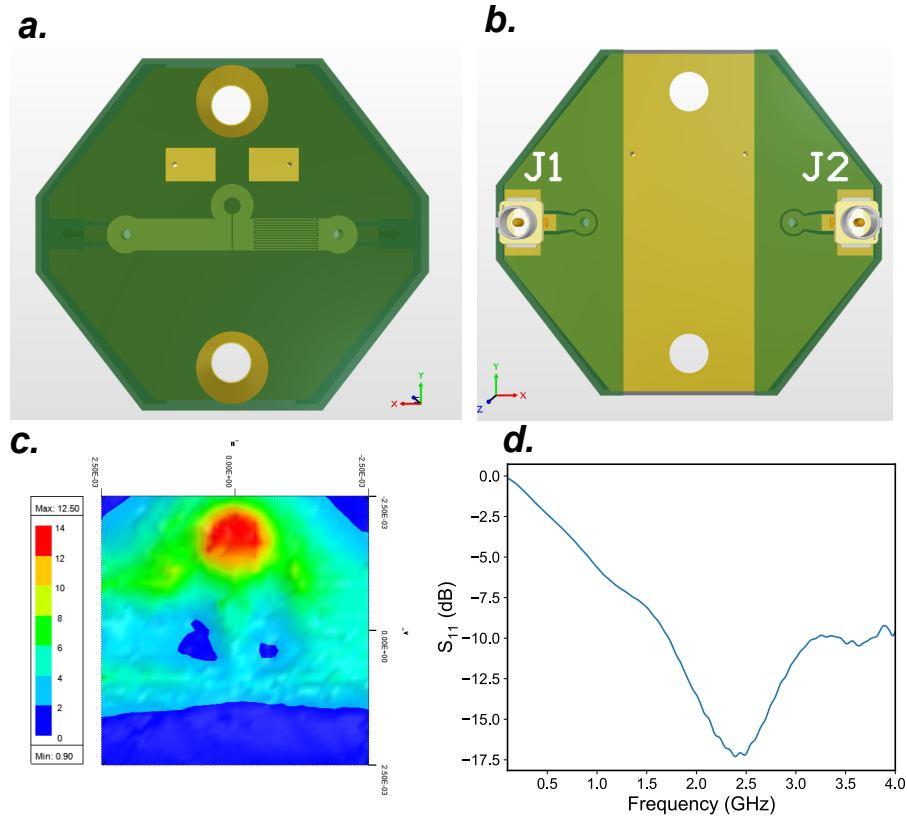


**Figure S5: PCB for microwave delivery.** For microwave delivery we designed a planar 50-Ohm transmission-line microstrip LC resonator consisting of a  $\Omega$ -loop planar inductor in series with an interdigitated planar capacitor (59, 60) fabricated onto a PCB (top view in (a), bottom view in (b)). The transmission line is terminated with a 50 Ohm resistor connected to J1 (shown in (b)) via a 50 Ohm coax cable, such that the impedance at the LC resonance frequency is 50 Ohms. The microstrip width and dimensions of the planar  $\Omega$ -loop inductor and interdigitated capacitor were determined by optimizing the simulated  $S_{11}$  in HFSS (Ansys) to obtain a broad LC resonance centered around  $\sim 2.7$  GHz matched to an input impedance of 50 Ohms. In (c) we show a HFSS simulation of the H-field near resonance at the surface of a 0.3mm thick diamond placed on top of the PCB, where we achieve a  $\sim 0.5$  mm<sup>2</sup> area of uniform maximum H-field above the center of the  $\Omega$ -loop. In cryogenic experiments, an area of the ground plane not covered with solder mask (large gold rectangular area at the center of the PCB in (b)) is mounted directly onto the cold finger of the cryostat contacted with silver paste. The ground plane is connected to two cooling pads through vias (gold rectangular areas above the  $\Omega$ -loop in (a)), which contact the diamond mounted on the top side of the PCB. In (d) we show  $S_{11}$  measured with a VNA (Agilent N5230A / N4431-60003) on a 50-Ohm terminated PCB manufactured from our design, which shows a broad LC resonance near 2.5 GHz.

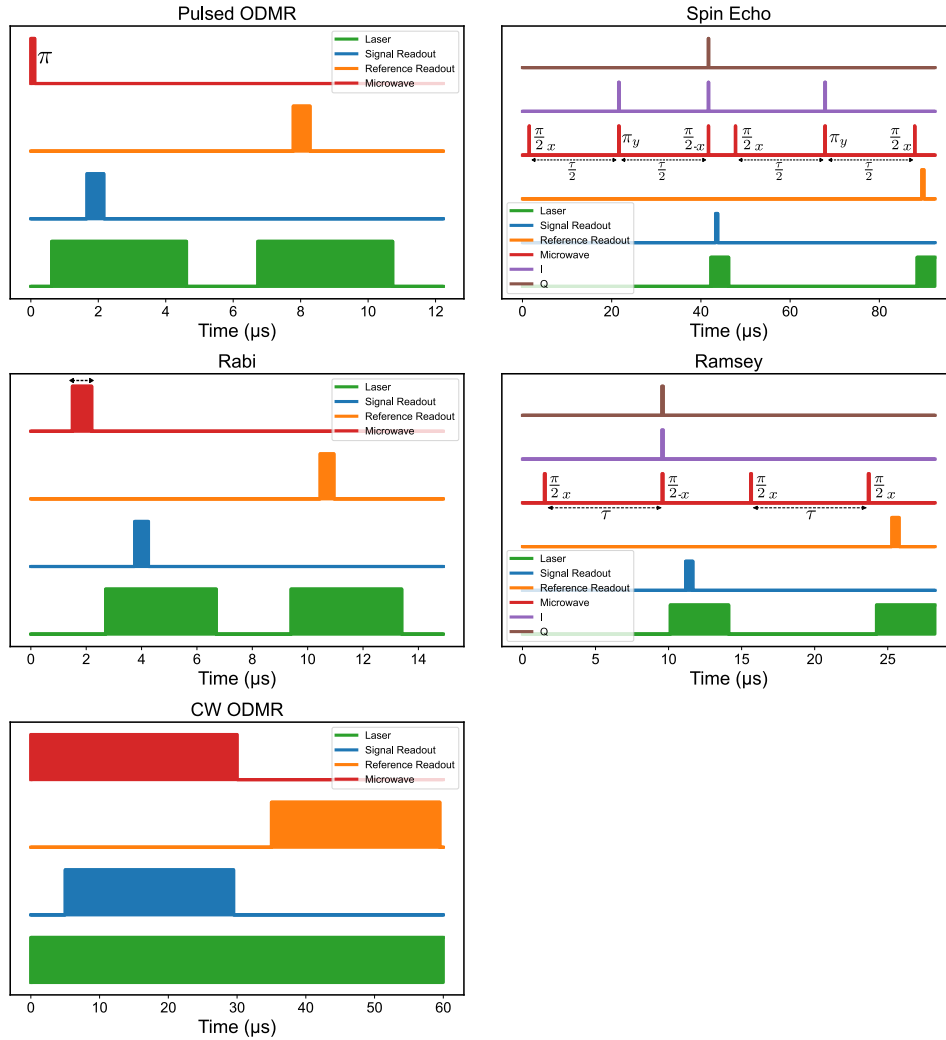


**Figure S6: Full pulse sequence diagrams.** Here we show the timing sequences for the TTL pulse outputs from channels of the PulseBlaster which control digital modulation of the AOM (labeled “Laser”), gating of the RF switch that feeds the microwave amplifier from the SG384/3 signal generator (labeled “Microwave”), gating of DAQ counter channels for signal and reference readout of the APD (labeled “Signal Readout” and “Reference Readout”), and gating of RF switches which feed a DC voltage into the I and Q modulation inputs of the SG384/3 signal generator (labeled “I” and “Q”). For pulsed ODMR, spin echo, Rabi, and Ramsey, the signal and reference readout pulses are set to  $500\text{ns}$  and laser pulses are set to a duration of  $4\mu\text{s}$ . A delay between the laser pulse onset and the signal and readout pulses is set to compensate for an electronic delay from the instruments (57). The I and Q modulation pulses are padded by  $20\text{ns}$  with respect to the  $\pi$  and  $\pi/2$  pulses in spin echo and Ramsey to compensate for the response time of the switches and SG384/3 IQ modulation (57).

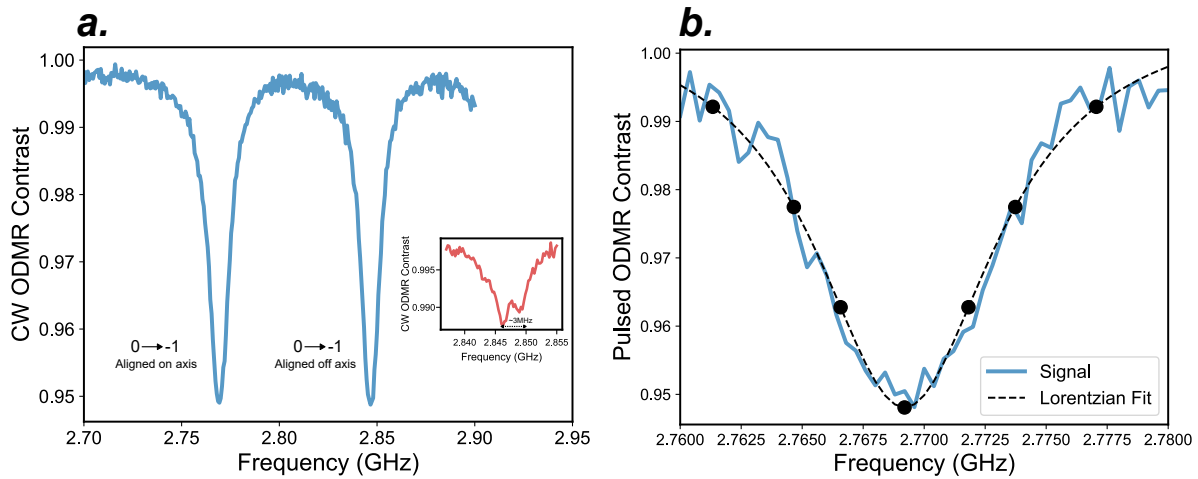


**Figure S7: NV magnetometry details.** (a) CW ODMR spectrum corresponding to alignment of the bias magnetic field along a  $[111]$  crystallographic axis of diamond. The ODMR peak labeled “Aligned on axis” corresponds to the  $|m_s = 0\rangle \rightarrow |m_s - 1\rangle$  resonance of NVs with their spin quantization axis oriented along the same direction as the bias field. (Inset) CW ODMR spectrum of the “off axis”  $|m_s = 0\rangle \rightarrow |m_s - 1\rangle$  resonance measured with low microwave power to resolve the overlap of the  $^{15}\text{N}$  hyperfine lines of NVs with spin quantization axes corresponding to the three “off axis”  $[111]$  orientations. (b) Pulsed ODMR spectrum of the “on axis”  $|m_s = 0\rangle \rightarrow |m_s - 1\rangle$  fit to a Lorentzian function, showing the seven measurement points that are selected for pulsed ODMR imaging (see Section 1.5 for details).



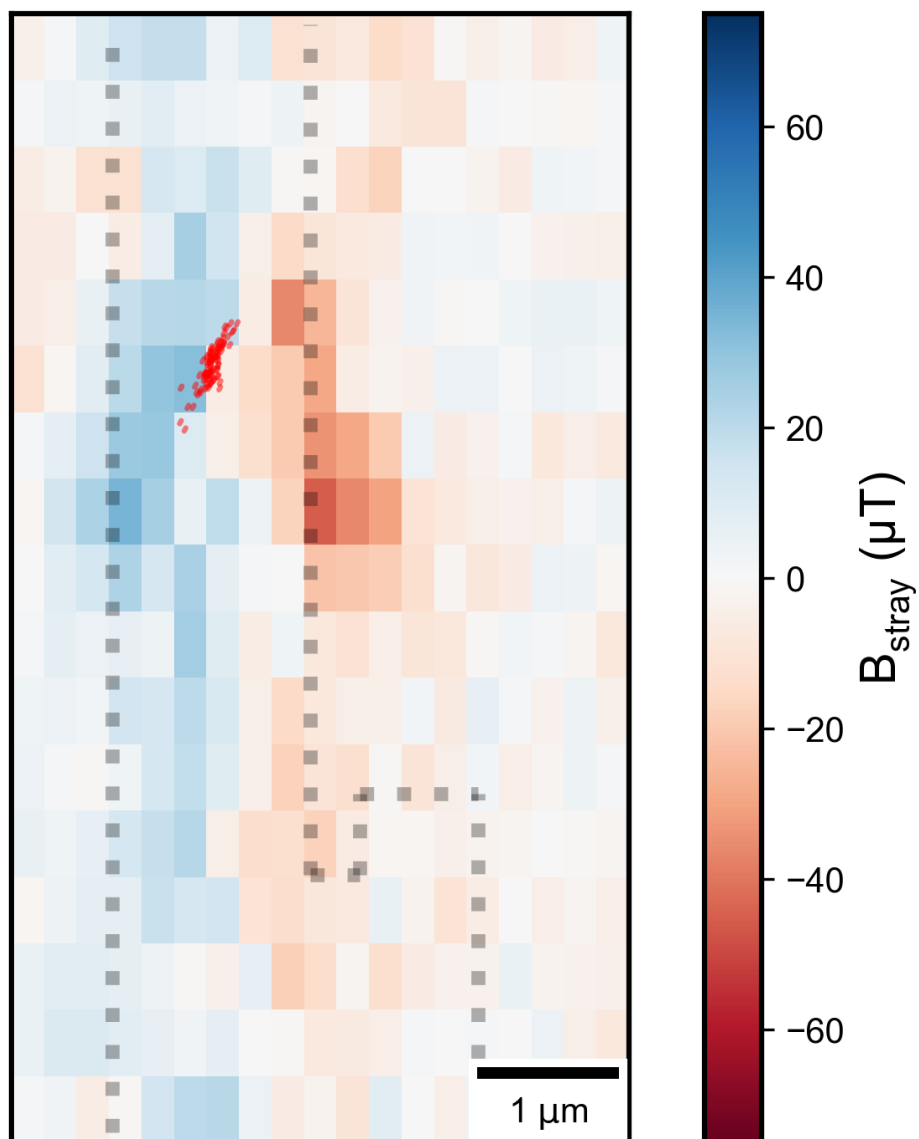


**Figure S8: Spread of points sampled in spin echo measurements with drift correction.** Pulsed ODMR stray field image recorded at 137.5  $K$  overlaid with the spread of points sampled in spin echo measurements at this temperature.

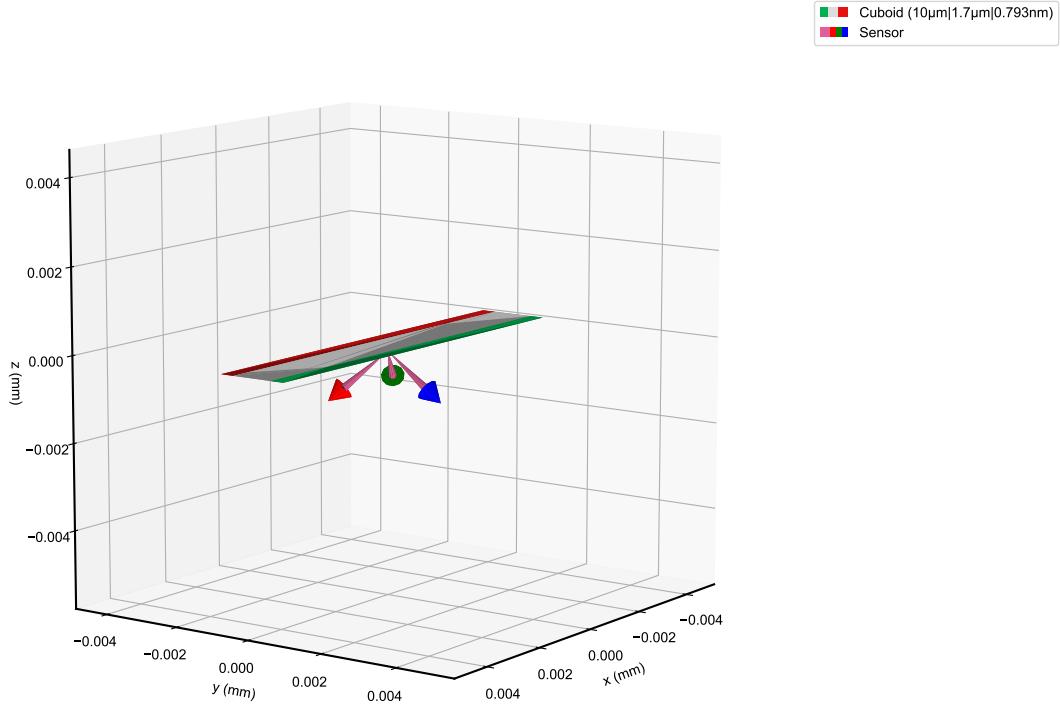


**Figure S9:  $B_{stray}$  simulation details.** We used MAGPYLIB (63) to simulate the stray magnetic fields from one uncompensated ferromagnetic monolayer of CrSBr. The geometry of the simulation set up is shown above. We defined the CrSBr flake as a cuboid with x,y dimensions of  $10 \mu m \times 1.7 \mu m$  and a z dimension of  $0.793 \text{ nm}$  corresponding to the thickness of one monolayer of CrSBr (26). The magnetization vector is oriented along y axis and its magnitude (the remanence) is calculated from the CrSBr unit cell magnetization at  $100 \text{ K}$  reported by López-Paz *et al.* (26) with the CrSBr unit cell volume. Experimentally, the CrSBr flake was oriented roughly so that the rectangular edges of the flake were parallel with the square edges of the diamond substrate during the transfer process such that x and y axes of the flake in the simulation are taken to point along [110] directions of the diamond unit cell, while the z axis corresponds to the [100] direction. We rotate the sensor coordinate system in the simulation such that the z-axis of the sensor (blue arrow in the figure above) in the new coordinate system points in a direction corresponding to the [111] direction of the diamond unit cell, i.e. along the NV spin quantization axis. The sensor is placed at a distance  $d$  below the flake and scanned in the x-y plane and the B-field projection onto the sensor z-axis is calculated to obtain a simulated image  $B_{sim}(x, y, d)$ . We then perform simulations of  $B_{sim}(x, y, d)$  over the range of  $d_{NV}$  spanned by the NV depth probability distribution function  $P(d_{NV})$  (Fig S2) and calculate an ensemble averaged image  $B_{sim_{ens}}(x, y) = \int B_{sim}(x, y, d_{NV})P(d_{NV}) dd_{NV}$ . Finally, the ensemble averaged image  $B_{sim_{ens}}(x, y)$  is convolved with a 2D Gaussian representing the optical diffraction limited width for a beam waist radius of  $\sim 500 \text{ nm}$  to generate the image shown in Fig 1d of the main text.

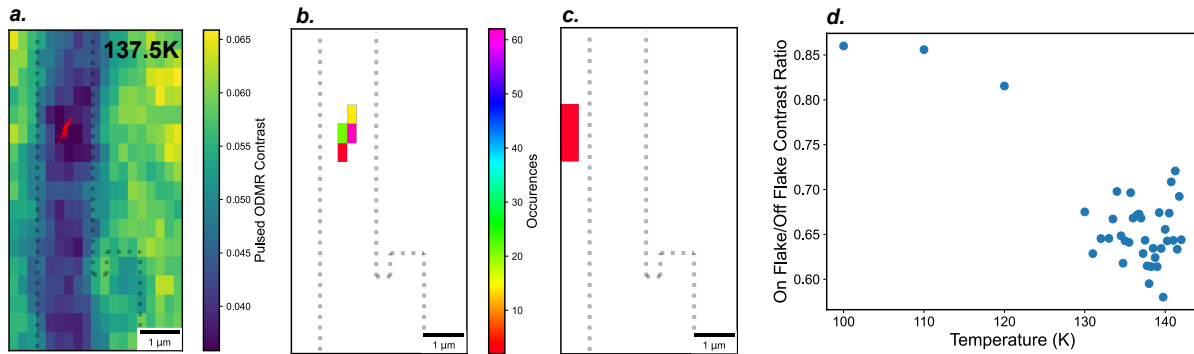


**Figure S10: Temperature dependence of on-flake vs. off-flake pulsed ODMR contrast**  
 (a) Pulsed ODMR contrast image (see Section 1.5) with points sampled during spin echo measurements overlaid in red. (b) Histogram of points sampled during spin echo measurements. (c) Pixels selected to evaluate “off-flake” pulsed ODMR contrast. (d) Ratio of pulsed ODMR contrast from “on-flake” vs. “off-flake” positions as a function of temperature.

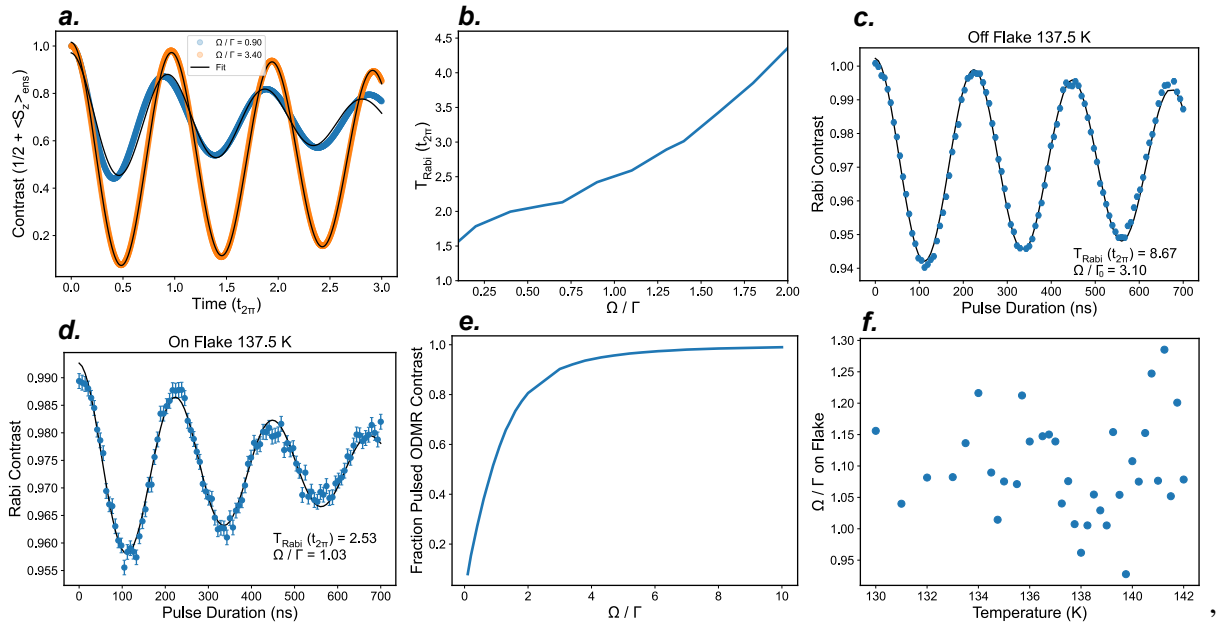


**Figure S11: Determining temperature dependence of  $\Omega/\Gamma$  across the CrSBr phase transition** (a) Simulated Rabi contrast for two values of  $\Omega/\Gamma$  with fits to Eq (S2). (b) Simulated  $T_{\text{Rabi}}$  as a function of  $\Omega/\Gamma$ . (c) & (d) Rabi oscillations measured at positions on and off the CrSBr flake at 137.5 K, from which  $T_{\text{Rabi}}$ ,  $\Omega/\Gamma$ , and  $\Omega/\Gamma_0$  are determined. (e) Simulated  $\pi$ -pulsed ODMR contrast as a function of  $\Omega/\Gamma$ . (f)  $\Omega/\Gamma$  at the position on the CrSBr flake sampled in spin echo measurements as a function of temperature.

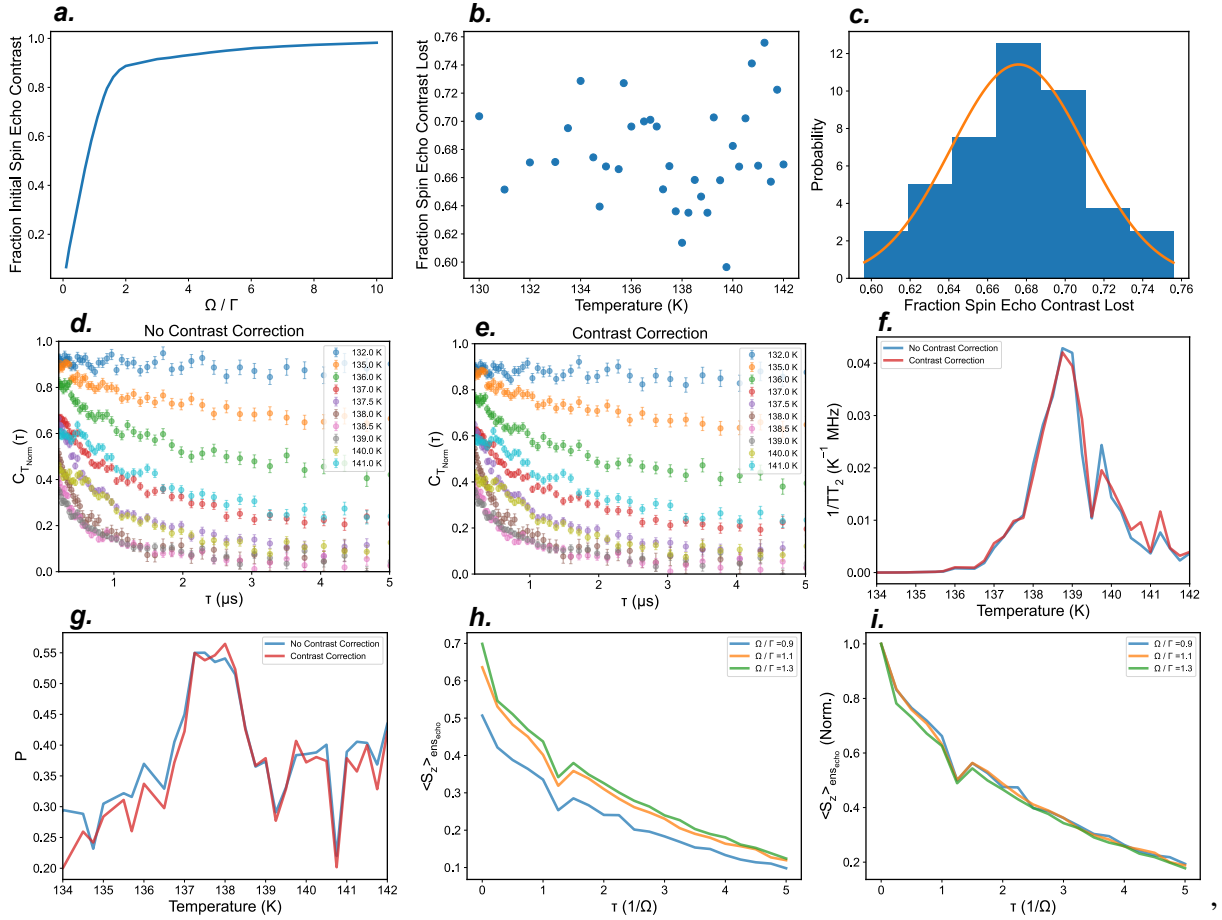


**Figure S12: Determining temperature dependence of spin echo contrast across the CrSBr phase transition.** (a) Simulated initial spin echo contrast as a function of  $\Omega/\Gamma$ . (b) Spin echo contrast lost as a function of temperature determined from the values of  $\Omega/\Gamma$  at the position on the CrSBr flake sampled in spin echo measurements. (c) Histogram of the spin echo contrast loss from (b) and fit to a normal distribution. (d), (e), (f), & (g) Comparisons of  $C_{T_{Norm}}(\tau)$  (for  $T_{Norm} = 131K$ ) and  $\frac{1}{T_2}$  and  $p$  stretched exponential fit parameters for raw spin echo data and for data corrected for a relative change in contrast based on (b). (h) & (i) Simulated spin echo coherence decays for different values of  $\Omega/\Gamma$ .

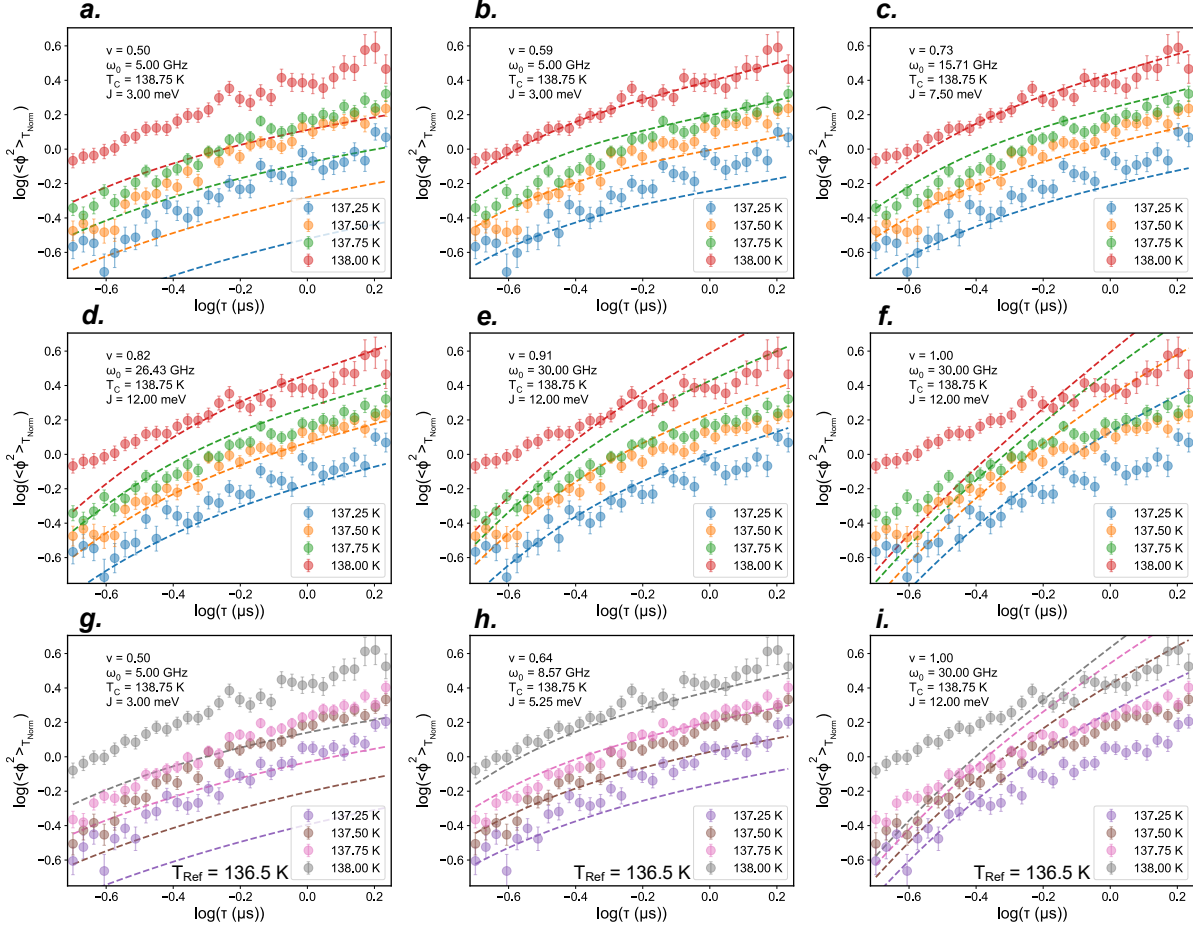


**Figure S13: Sensitivity of critical dynamics simulations to the value of  $\nu$ .** To determine the sensitivity of the fits to the parameter  $\nu$ , we fixed  $\nu$  to values in the range of 0.5-1 (note  $\nu_{\text{Ising}} = 1$ ) and allowed the parameters  $J$  and  $\omega_0$  to vary within reasonable ranges for the simulations of  $\langle \phi^2 \rangle_{T_{\text{Norm}}}^{\text{ens}}$  using  $T_C = 138.75 \text{ K}$  and  $T_{\text{Ref}} = 136.75 \text{ K}$ . (a), (b), (d-f) Fits with the parameter  $\nu$  fixed at 0.5, 0.59, 0.82, 0.91, and 1, respectively, whereas (c) shows the fits from Figure 4a in the main text with  $\nu$  allowed to vary to a best fit value of  $\nu = 0.73$ . Only fits with fixed values of  $\nu$  in the range of  $\sim 0.6 - 0.8$  can reproduce the trend of the data. Note that the fits in (f) correspond to the Ising trends shown in Figure 4a of the main text. We also evaluate the sensitivity of the fits to  $\nu$  using a different  $T_{\text{Ref}} = 136.5 \text{ K}$  near criticality (g-i). (g) & (i) Fits with  $\nu$  fixed at 0.5 and 1, respectively; (h) shows a fit with  $\nu$  allowed to vary to a best fit value of  $\nu = 0.64$ .